A Fast Vector Radiative Transfer Model for the Atmosphere-Ocean Coupled System

Jiachen Ding[1], Ping Yang[1],
Michael D. King[2,1], Steven Platnick[3], Xu Liu[4], Kerry G. Meyer[3], Chenxi Wang[5]

[1]Department of Atmospheric Sciences, Texas A&M University, College Station, TX 77845, USA
[2]Laboratory for Atmospheric & Space Physics, University of Colorado, CO 80303, USA
[3]Earth Sciences Division, NASA Goddard Space Flight Center, Greenbelt, MD 20771, USA
[4]NASA Langley Research Center, Hampton VA
[5]University of Maryland, College Park, MD, USA

Abstract

To infer atmospheric and oceanic constituent properties from polarimetric observations, an efficient and accurate retrieval algorithm is desirable. In-line radiative transfer calculations are indispensable if a large state vector, including both atmospheric profiles and surface properties, is used to improve retrieval accuracy. However, in-line radiative transfer calculations are usually not computationally efficient for remote sensing applications. Therefore, there is a pressing need to develop an accurate and fast vector radiative transfer model (RTM) to fully utilize satellite polarimetric observations.

This paper reports on a fast vector RTM, referred to as TAMU-VRTM, in support of polarimetric remote sensing, which is capable of simulating the Stokes vector values observed at the top of the atmosphere and at the surface by fully considering absorption, scattering, and emission in the atmosphere and ocean. Gaseous absorption is parameterized with respect to gas concentration, temperature, and pressure, by using a regression method applicable to an inhomogeneous atmospheric path. An efficient two-component approach combining the small-angle approximation and the adding-doubling method is utilized to solve the vector radiative transfer equation (RTE). The thermal emission component of the RTE solution is obtained by an efficient doubling process. The air-sea interface is treated as a wind-ruffled rough surface in the model to mimic a realistic ocean surface. Several oceanic optical property models are introduced to model ocean inherent optical properties. To demonstrate the applicability of the TAMU-VRTM, simulations are compared with satellite observations, and results from other vector radiative transfer methods including benchmarks.

Keywords: radiative transfer in coupled atmosphere-ocean system; polarimetric remote sensing; parameterization of gaseous absorption; small-angle approximation; air-sea interface

1. Introduction

In spaceborne and airborne remote sensing of the atmosphere and ocean, it is necessary to use a radiative transfer model (RTM) to simulate the radiometric or polarimetric quantities observed by a satellite sensor under various atmospheric and oceanic conditions. Polarimetric remote sensors, not only measure the radiance, but also measure the state of polarization of the radiation reflected and emitted by cloud, aerosol, and oceans. Polarization contains rich information about the medium (e.g., the atmosphere and ocean) that the radiation interacted with. The feasibility and intrinsic merit of spaceborne and airborne polarimetric remote sensing has been demonstrated (e.g., [1-3]). In particular, the observations by the Polarization and Directionality of the Earth's Reflectances (POLDER) [4] and Airborne Multiangle SpectroPolarimetric Imager (AirMSPI) [5] can be used to effectively infer cloud, aerosol and ocean properties. POLDER and AirMSPI observe reflected solar radiation in visible (VIS) to near-IR (NIR) bands. Recent studies [6-7] show that spaceborne and airborne microwave/submillimeter polarimetric radiometers such as the Global Precipitation Measurement Microwave Imager (GPM-GMI) [8] and Compact Scanning Submillimeter-wave Imaging Radiometer (CoSSIR) [9] have considerable potential for measuring the microphysical properties of ice clouds by observing thermal emission from the earth-atmosphere system. In addition, future satellite missions such as the Plankton, Aerosol, Cloud, ocean Ecosystem (PACE) [10], the Multi-Angle Imager for Aerosol (MAIA) [11], Aerosol/Cloud/Ecosystem mission (ACE) [12] and the Multi-viewing-

channel-polarisation Imager (3MI) [13] will deploy more advanced polarimeters. In addition to enhanced polarimetric capabilities, these future instruments will have higher spectral and spatial resolutions. The tremendously enhanced data to be obtained from the future instruments will contain much more information about the atmosphere and oceans such as aerosol composition and phytoplankton characterization. To fully exploit the polarimetric capability of the new instruments, it is imperative to incorporate an efficient and accurate vector RTM into the retrieval algorithms.

For practical applications, a vector RTM must be able to account for the absorption and emission by atmospheric gases. At present, most fast hyperspectral RTMs (e.g., [14-16]) are limited to clear-sky cases where only gaseous absorption and emission, and the surface reflection and emission contribute to radiation obtained at the top of the atmosphere (TOA). Some fast hyperspectral RTMs (e.g., [17-19]) and broadband RTMs (e.g., [20]) consider both gaseous absorption and multiple scattering in aerosol and cloud layers. However, these models do not consider the polarization state of radiation. Polarimetric remote sensing certainly requires an appropriate RTM to account for the polarization state of the radiation field. Without consideration of polarization, radiative transfer (RT) calculations have varying degrees of inaccuracy, depending on specific applications. For example, in a Rayleigh scattering atmosphere, neglecting polarization can result in errors up to 10% even for radiance simulations [21-22]. The errors are much larger than the instrument calibration error and noise level. The errors have a complex dependence on viewing geometry and optical thickness; as a result, it is difficult to empirically correct the errors [22].

In this study, we develop a fast vector RTM (hereafter, TAMU-VRTM) for applications to atmospheric and oceanic remote sensing. Compared with previously developed RTMs for remote sensing purpose, the TAMU-VRTM can fully account for polarization from solar to thermal infrared bands using an efficient and flexible vector radiative transfer equation (RTE) solver. The gaseous absorption transmittance is accurately and efficiently computed using a newly developed gaseous absorption parameterization scheme. The TAMU-VRTM is a useful tool for simulating observations of remote sensing instruments, which will potentially benefit retrievals of aerosol, cloud, and oceanic properties from the PACE, MAIA, ACE and 3MI observations. In addition, the TAMU-VRTM can also improve remote sensing techniques based on the existing POLDER, AirMSPI, Moderate Resolution Imaging Spectroradiometer (MODIS) [23] and Visible Infrared Imaging Radiometer Suite (VIIRS) instruments [24]. In this paper, we introduce the main modules of the TAMU-VRTM, and show its potential capabilities. Section 2 presents an overview of the developed model. Sections 3-6 describe the details of the model. Section 7 shows computational results and comparisons with satellite observation. Section 8 summarizes the study.

2. An Overview of the RTM

2.1 Model Layer Setup and Geometry

The TAMU-VRTM is capable of simulating the full Stokes vector with variable spectral resolution under various atmospheric and oceanic conditions. The TAMU-VRTM is based on a plane-parallel approximation, and is a one-dimensional model. In particular, the atmosphere is divided into a number of homogeneous layers. However, these layers may be different. Each layer composition includes gases, and possibly clouds, aerosols, or a mixture. The ocean layer of Case I water contains pure water, phytoplankton, non-algae particles (NAP) and Colored

Dissolved Organic Matter (CDOM) [25]. There is an interface between the atmosphere and ocean. The absorption, scattering and emission by the atmosphere and ocean are considered in the calculation.

The vector RTE under macroscopically isotropic and mirror-symmetric particulate media [26-27], and with the plane-parallel approximation is written as

$$u\frac{\partial \mathbf{I}(\tau,u,\varphi)}{\partial \tau}=\mathbf{I}(\tau,u,\varphi) \\ -\frac{\varpi(\tau)}{4\pi}\int_{-1}^{1}du'\int_{0}^{2\pi}d\varphi'\mathbf{P}(\tau,u,u',\varphi-\varphi')\mathbf{I}(\tau,u',\varphi')-\left[1-\varpi(\tau)\right]\mathbf{B}\left[T(\tau)\right], \tag{1}$$

where $\mathbf{I}$ is the Stokes vector, $\mathbf{P}$ is the phase matrix, $\mathbf{B}$ is the Planck function vector, and ϖ is the single-scattering albedo, T is temperature, τ is optical thickness, u is the cosine of zenith angle, and φ is the azimuth angle. The wavelength dependences of $\mathbf{I}$, $\mathbf{P}$, $\mathbf{B}$, τ and ϖ are implied but not explicitly denoted in Eq. (1). $\mathbf{B}$ is $\begin{pmatrix} B\left[T(\tau)\right] & 0 & 0 & 0 \end{pmatrix}^{\mathrm{T}}$, in which superscript 'T' denotes matrix transpose, and B is the Planck function.

Incident and outgoing zenith angles (θ' and θ), and incident and outgoing azimuth angles (φ' and φ) describe the viewing geometry. The zenith angle is in the interval (0, π). The zenith angle is the angle between zenith and beam propagation directions. The azimuth angle is the angle between the x-axis and the horizontal projection of the beam propagation direction, which is measured clockwise when looking along the zenith direction. The azimuth angle is in the interval (0, 2π). The relative azimuth angle $\Delta\varphi=\varphi-\varphi'$ is in the interval (0, π) due to symmetry with respect to $\Delta\varphi=\pi$. The absolute value of the cosine of the zenith angle $\mu=|u|$ is also used to describe polar directions. μ and $-\mu$ specify upward and downward directions respectively. One exception is the solar zenith angle μ_0. Although the incident solar radiation is always downward in a plane-parallel atmosphere, μ_0 rather than $-\mu_0$ specifies its direction.

2.2 Channel-averaged radiative transfer

The Stokes vector in Eq. (1) can be written as $\mathbf{I}=\mathbf{I}_{\mathrm{s}}+\mathbf{I}_{\mathrm{t}}$. $\mathbf{I}_{\mathrm{s}}$ and $\mathbf{I}_{\mathrm{t}}$ are the solution components when solar radiation and thermal emission by the atmosphere and the surface are sources. Because Eq. (1) is a linear integro-differential equation, it can be written as two decoupled equations,

$$u\frac{\partial \mathbf{I}_{\mathrm{s}}(\tau,u,\varphi)}{\partial \tau}=\mathbf{I}_{\mathrm{s}}(\tau,u,\varphi) \\ -\frac{\varpi(\tau)}{4\pi}\int_{-1}^{1}du'\int_{0}^{2\pi}d\varphi'\mathbf{P}(\tau,u,u',\varphi-\varphi')\mathbf{I}_{\mathrm{s}}(\tau,u',\varphi'), \tag{2a}$$

$$u\frac{\partial \mathbf{I}_{\mathrm{t}}(\tau,u,\varphi)}{\partial \tau}=\mathbf{I}_{\mathrm{t}}(\tau,u,\varphi) \\ -\frac{\varpi(\tau)}{4\pi}\int_{-1}^{1}du'\int_{0}^{2\pi}d\varphi'\mathbf{P}(\tau,u,u',\varphi-\varphi')\mathbf{I}_{\mathrm{t}}(\tau,u',\varphi')-\left[1-\varpi(\tau)\right]\mathbf{B}\left[T(\tau)\right]. \tag{2b}$$

Equations (2a) and (2b) can be solved separately so the sum of their solutions is the total Stoke vector of the radiation field. In the ultraviolet (UV) to NIR bands, the atmospheric thermal emission is very small compared to the solar radiation and is neglected so the contribution by

thermal emission to the solution is zero. Similarly, in the far infrared to microwave band or at night, solar radiation can be neglected in Eq. (2a). The solar radiation or thermal emission is neglected when their contributions are below the specified noise level.

Satellite instruments receive the channel-averaged radiance defined as

$$\overline{I} = \int_{\nu_1}^{\nu_2} I(\nu) S(\nu) d\nu , \tag{3}$$

where $\overline{I}$ is the channel-averaged radiance, $I(\nu)$ is the radiance at wavenumber ν, and $S(\nu)$ is the normalized spectral response function (SRF) of the receiver at wavenumber ν. The optical properties of cloud, aerosol and ocean usually vary slightly in the spectral range of a band with moderate and higher spectral resolution such as most of the MODIS and POLDER bands. However, the absorption by atmospheric gases varies considerably even in a narrow spectral range. An accurate way to compute the integral $\overline{I}$ with Eq. (3) is sampling a large number of monochromatic wavenumbers in a given narrow band. However, this approach is computationally inefficient and impractical as an in-line RTM. Instead, we utilize channel-averaged RT calculation as an approximation to Eq. (3). The optical properties (i.e. absorption, scattering and emission) of the model atmosphere and ocean are averaged in the spectral range of a channel. Thus, radiative transfer calculation is needed only once to obtain approximate channel-averaged radiance $\overline{I}$. The channel-averaged optical property is defined as

$$\overline{X} = \int_{\nu_1}^{\nu_2} X(\nu) S(\nu) d\nu , \tag{4}$$

where X and $\overline{X}$ indicate an arbitrary optical property and its channel-averaged counterpart, respectively.

In some spectral bands such as in shortwave IR (SWIR) bands with certain width, the optical properties of cloud, aerosol and surface may also have significant variations, and we can divide a band into some subbands and do RT calculation at each subband [28] to improve the accuracy.

2.3 Introduction to Each Module in the RTM

2.3.1 Gaseous Absorption

Gaseous absorption is a critical process in radiative transfer. We consider channel-averaged transmittance (CAT) in the channel-averaged radiative transfer calculation, defined in a transmission path as

$$\overline{t} = \int_{\nu_1}^{\nu_2} S(\nu) \exp[-\tau_\nu(\nu)] d\nu , \tag{5}$$

where τ_ν is the monochromatic optical thickness of gaseous absorption along the transmission path. τ_ν is a function of wavelength as well as gas concentration, pressure and temperature. The integral in Eq. (5) can be evaluated by using the line-by-line (LBL) method [29] that is time-consuming. In other words, the LBL method is impractical due to a tremendous computational burden. Because of the complicated dependence of CAT on atmospheric profiles, we perform CAT computation as part of the TAMU-VRTM.

Many research efforts have been devoted to efficient and accurate computation of CAT (also called spectral transmittance if the SRF is ignored) such as band-model approaches (e.g., [30-37]), the correlated k-distribution method (CKD) (e.g., [20, 38-42]), regression-based

methods (e.g., [14, 43-44]), the Principal Component Radiative Transfer Model (PCRTM) [15, 19], and the Optimal Spectral Sampling (OSS) method [16].

Among the approaches mentioned above, the band-model approaches do not precisely account for a detailed SRF and may not be sufficiently accurate for remote sensing applications. It is difficult to constrain the errors caused by the correlation assumption for an inhomogeneous atmosphere. The regression-based methods have been proven accurate and efficient in many operational retrieval algorithms, and are relatively easy to implement. Thus, we develop a regression-based algorithm to compute CAT. The regression-based method does not have correlation assumption errors in CKD methods. It is straightforward to control the regression error by designing proper regression equation and predictors. Also, if a band has several absorptive gases, the CKD method usually assumes the absorption lines to be uncorrelated, which may incur some errors. The regression-based method can handle the line overlap problem without any assumptions by applying regressions for each absorptive gas and attain the accuracy of the simulated CAT. The previous regression-based methods perform regression in a layer-by-layer form. In the present method, we only perform one regression for an inhomogeneous atmospheric path, which is more efficient, particularly for solar bands. The details will be discussed in section 3.

2.3.2 Multiple Scattering

Both Eqs. (2a) and (2b) contain a multiple scattering term. An efficient vector RTE solver is needed to account for multiple scatterings in cloud, aerosol and ocean layers. The Successive Order of Scattering (SOS) method (e.g., [45-47]), the Adding-Doubling (AD) method (e.g., [48-50]), the Discrete Ordinate (DO) method (e.g., [51-57]) and the Monte Carlo (MC) method (e.g., [58-59]) are widely used in solving a vector RTE. In the present model, we use the AD method [60] to solve the vector RTE, because it is numerically stable and easily accounts for multiple layers.

The phase matrices of atmospheric and oceanic particles are highly anisotropic. Especially in the forward direction, the diagonal elements of the phase matrix always have strong forward peaks. Thus, a large number of expansion terms are needed to represent the phase matrix accurately in terms of general spherical functions (GSF) [61]; as a result, the corresponding radiative transfer calculations are computationally inefficient. To overcome this difficulty, several approaches are developed to truncate the forward peak in the phase function (e.g., [62-65]) and the phase matrix (e.g., [66-68]) so that fewer GSF terms are needed in radiative transfer calculations to attain decent accuracy. Some correction methods such as the TMS and IMS methods [69] are also developed to correct the single-scattering errors caused by the truncation operation.

Previous studies [e.g. 68, 70-71] show that the errors caused by the Delta-M truncation method (DMM) [63] and Delta-Fit truncation method (DFM) [64] can be substantially reduced by the TMS single-scattering correction method. However, the forward scattering may be overestimated during the single-scattering correction process, since an extra source term is introduced into the forward direction [68]. Although for a solar source, remote sensing instrument only receives radiation in the backward hemisphere in the scattering domain, an accurate radiative transfer calculation in forward directions is still necessary, because it affects the simulation in reflection directions under certain conditions. For example, the reflection of forward transmitted solar radiation by the sea surface leads to sun glint that is received by airborne or spaceborne instruments. The sun glint phenomenon has been utilized to measure sea

surface characteristics [72] and proved to contain rich information about aerosol properties [73] such as aerosol absorption [74]. Coupled with polarimetric observation, sun glint is useful in detecting ocean surface oil slicks [75]. Also, transmitted solar radiation through the air-sea interface accounts for as much as 30% of the polarization of water-leaving radiance [76]. Thus, a method is needed to keep both reflection and transmission accurate while significantly improving the numerical efficiency of solving the vector RTE.

Lin et al. [77] accurately simulate the sun glint signal using the DO method with DMM and TMS single-scattering correction (DMM&TMS), and shows that although the direct solar beam reflection contributes to a large amount of sun glint signal, the diffuse radiation contribution from multiple scattering by the atmosphere cannot be neglected in sun glint simulation. In this study, a two-component method is developed to solve the vector RTE, which can avoid potential overestimation of forward scattering by DMM&TMS when there is a thin cloud that has very strong forward peak. In the two-component method, the highly anisotropic phase matrix of atmospheric and oceanic particles is decomposed into the forward and diffuse components. The forward component is nonzero only in a small angular range. The diffuse component is much more isotropic. Similarly, the Stokes vector of the RTE solution is also decomposed into forward and diffuse components. The decompositions of the scattering phase matrix and Stokes vector give forward and diffuse RTEs. The forward solution serves as source of the diffuse RTE. The forward Stokes vector and scattering phase matrix in the diffuse RTE are approximated by the Dirac Delta function, so the forward and diffuse RTEs are decoupled. The forward RTE is solved by the small-angle approximation (SAA) method [78]. The diffuse RTE is solved by the AD method [60]. The AD computation is substantially accelerated due to the fact that the diffuse phase matrix can be expanded with a much lower order of the GSF. The detailed description is given in section 4.

2.3.3 Thermal Emission

In Eq. (2b), the thermal emission comes from the atmosphere and the surface. In a clear-sky condition, Eq. (2b) can be solved if we know the CAT and temperature of each layer. If scattering layers are present, thermal emission experiences multiple scattering. Previous studies [79-81] discuss multiple scattering calculations in the AD method when thermal emission is involved. However, none of them consider the state of polarization. In this study, we develop an efficient thermal emission computational approach incorporated into the AD method. The approach is illustrated in section 5.

2.3.4 Air-Sea Interface and Ocean Model

The radiative transfer processes in the atmosphere and oceans are coupled through the air-sea interface. The vector RTE is solved for the atmosphere-ocean system (AOS). The SOS method is one of the most popular vector RTE solver of an AOS (e.g., [47, 82-83]). Other AOS vector RTE solvers include the MC method (e.g., [76]), the matrix-operator method (e.g., [53, 84]), the DO method (e.g., [55-57]) and the AD method (e.g., [25]). In this study, we extend the AD vector RTE solver by Huang et al. [60] to an AOS. The air-sea interface is assumed to be a rough surface in the model to mimic the realistic ocean surface. The transmission and reflection properties of the interface are related to the ocean surface condition including sea surface wind speed and direction, and albedo.

Pure water, phytoplankton, NAP and CDOM are included in the model of ocean inherent optical property (IOP) computation. Currently, only one homogeneous ocean layer is considered in the model. The details are described in section 6.

3. Gaseous Absorption Calculation

3.1 Methodology

As illustrated in section 2, CAT is needed for channel-averaged radiative transfer calculation concerning absorptive atmospheric gases. In a clear-sky atmosphere, if Rayleigh scattering is neglected and ϖ is equal to zero, the solution to the vector RTE Eq. (2) can be written as,

$$\mathbf{I}_{\mathrm{s}}\left(0,\mu,\varphi\right)=\frac{\mu_0 F_0}{\pi}\overline{t}_{l_s\sim 1}(\mu_0)\mathbf{R}_{\mathrm{surf}}\left(\mu_0,\varphi_0,\mu,\varphi\right)\begin{pmatrix}1&0&0&0\end{pmatrix}^{\mathrm{T}}\overline{t}_{l_s\sim 1}(\mu), \tag{6a}$$

$$\mathbf{I}_{\mathrm{t}}\left(0,\mu,\varphi\right)=\varepsilon_{\mathrm{surf}}\mathbf{B}(T_{\mathrm{surf}})\overline{t}_{l_s\sim 1}(\mu)+\sum_{l=1}^{l_s}\mathbf{B}(T_l)\left[\overline{t}_{(l-1)\sim 1}(\mu)-\overline{t}_{l\sim 1}(\mu)\right], \tag{6b}$$

where F_0 is solar flux, $\mathbf{R}_{\mathrm{surf}}$ is the reflection matrix at the surface, φ_0 is solar azimuth angle, $\varepsilon_{\mathrm{surf}}$ is surface emissivity, T_{surf} is surface temperature, and l_s is the number of layers from the surface to TOA. l_s is smaller or equal to the total number of layers in the model. The first layer is at the TOA. The last layer is the bottommost layer. $\overline{t}_{l\sim 1}$ is the CAT from the layer l to the layer 1. The model has up to 100 atmospheric pressure layers corresponding to 101 pressure levels ranging from 0.005 hPa to 1100 hPa to be consistent with the pressure layer setup in [14]. In a clear-sky atmosphere, as indicated in Eq. (6), the layer-to-TOA CATs are needed in the channel-averaged RT calculation for a thermal emission source. Similarly, for a solar incidence source, the surface-to-TOA CAT is needed. If there are scattering layers, we also need CATs among scattering layers, the surface and TOA as well as CATs within the scattering layers. Therefore, the gaseous absorption calculation module should be able to compute layer-to-layer CATs between two arbitrary layers in the model to account for various atmospheric conditions.

The layer-to-layer CAT is defined as

$$\overline{t}_{i\sim j}=\sum_{m=1}^{M}S_m\exp\left[-a\sum_{l=i}^{j}\tau_m^l\right], \tag{7}$$

where $\overline{t}_{i\sim j}$ is the CAT from layer i to layer j. M is the number of wavenumber points considered in the spectral range. S_m is the discretized SRF at the m-th wavenumber in the spectral range. τ_m^l is the monochromatic optical thickness in the layer l at the m-th wavenumber. a is the secant of the zenith angle ($1/\mu$). $\overline{t}_{i\sim j}$ is a function of gas concentration, temperature, pressure and a. We develop a regression approach to parameterize the layer-to-layer CAT with atmospheric variables (e.g., pressure, temperature and gas concentrations). It can be seen from Eq. (7) that $\overline{t}_{i\sim j}$ exponentially depends on monochromatic optical thickness, but the optical thickness is linearly proportional to gas concentration, for which it is difficult to directly parameterize CAT with respect to atmospheric variables. Alternatively, we define the layer-to-layer channel-averaged optical thickness (CAOT) as

$$\overline{\tau}_{i\sim j}\equiv-\ln\overline{t}_{i\sim j}, \tag{8}$$

which is parameterized with respect to atmospheric variables.

Eight gases are considered in the absorption calculation, namely, water vapor (H_2O), carbon dioxide (CO_2), ozone (O_3), nitrous oxide (N_2O), carbon monoxide (CO), methane (CH_4), oxygen (O_2), and nitrogen (N_2). Two kinds of absorption are considered: line absorption by H_2O, CO_2, O_3, N_2O, CO, CH_4, and O_2, and continuum absorption by H_2O, CO_2, O_3, O_2 and N_2. If more than one gas is an absorber in a channel, the CAOTs of all the gases are parameterized and computed separately, and then combined to obtain total CAOT. Note that the total CAOT is not equal to the sum of CAOTs of each gas, because Beer's law is invalid for CAT. To keep the total CAOT correct, we define the CAOT of each gas as

$$\begin{aligned} &\overline{\tau}_{i\sim j,1} \equiv \overline{\tau}_{i\sim j,1\sim N} - \overline{\tau}_{i\sim j,2\sim N}, \\ &\overline{\tau}_{i\sim j,2} \equiv \overline{\tau}_{i\sim j,2\sim N} - \overline{\tau}_{i\sim j,3\sim N}, \\ &\cdots, \\ &\overline{\tau}_{i\sim j,N-1} \equiv \overline{\tau}_{i\sim j,N-1\sim N} - \overline{\tau}_{i\sim j,N}. \end{aligned} \quad , \tag{9}$$

where N is the number of absorptive gases in the channel. The second subscript in each CAOT is the index of the gas in the CAOT calculation. For example, $\overline{\tau}_{i\sim j,1\sim N}$ is the CAOT for gases 1, 2, … N, while $\overline{\tau}_{i\sim j,N}$ is the CAOT of the single gas N. The CAOTs on the right-hand side of Eq. (9) are computed by the Line-by-line Radiative Transfer Model (LBLRTM) [29]. The total CAOT is

$$\overline{\tau}_{i\sim j,tot} \equiv \overline{\tau}_{i\sim j,1\sim N} = \sum_{n=1}^{N} \overline{\tau}_{i\sim j,n} . \tag{10}$$

The next step is to find a relation between $\overline{\tau}_{i\sim j,n}$ and the atmospheric variables, and use a polynomial regression approach to quantify this relation. To make regression numerically stable, we define the relative CAOT of a single gas n as,

$$\overline{\tau}_{r,i\sim j,n} \equiv \frac{\overline{\tau}_{i\sim j,n}}{\overline{\tau}_{ref,i\sim j,n}}, \tag{11}$$

in which $\overline{\tau}_{ref,i\sim j,n}$ is the reference CAOT of single gas n computed in conjunction with the U.S. standard atmospheric profile. $\overline{\tau}_{r,i\sim j,n}$ is a function of atmospheric temperature, pressure, and gas concentrations in layers i to j,

$$\overline{\tau}_{r,i\sim j,n} = \overline{\tau}_{r,i\sim j,n}\left(T_i, T_{i+1}, \cdots, T_j \mid P_i, P_{i+1}, \cdots, P_j \mid u_{i,n}, u_{i+1,n}, \cdots, u_{j,n}\right), \tag{12}$$

in which T_i is the temperature of layer i, P_i the pressure of layer i, and $u_{i,n}$ the concentration of gas n in layer i.

With a trial-and-error method, we construct a polynomial equation to parameterize $\overline{\tau}_{r,i\sim j,n}$,

$$\overline{\tau}_{r,i\sim j,n} = \sum_{k=1}^{K}\sum_{h=0}^{H} c_{kh}\left(\mathrm{G}_{i\sim j,n}^{\gamma}\right)^k\left(\mathrm{T}_{i\sim j}\right)^h , \tag{13}$$

in which $\mathrm{G}_{i\sim j,n}$ is the gas n concentration predictor. The exponent γ ranges from 0 to 1. $\mathrm{T}_{i\sim j}$ is the temperature predictor. c_{kh} is a polynomial coefficient. K can be 1, 2, 3, or 4; H can be 0, 1, 2 or 3. K and H are determined to satisfy accuracy and computation speed requirements.

$\mathrm{T}_{i\sim j}$ is the sum of pressure-weighted temperature divided by its counterpart for a reference atmospheric profile,

$$\mathrm{T}_{i\sim j}=\left(\sum_{l=i}^{j}T_l P_l\right)\Big/\left(\sum_{l=i}^{j}T_{ref,l}P_l\right), \tag{14}$$

where $T_{ref,i}$ is the layer *i* temperature in the reference atmospheric profile.

$\mathrm{G}_{i\sim j,n}$ is the sum of weighted gas concentration divided by its counterpart for a reference atmospheric profile. $\mathrm{G}_{i\sim j,n}$ has different forms for various gases at various channels, such as, unweighted gas concentration:

$$\mathrm{G}^{0}_{i\sim j,n}=\left(\sum_{l=i}^{j}u_{l,n}\right)\Big/\left(\sum_{l=i}^{j}u_{ref,l,n}\right), \tag{15a}$$

pressure-weighted gas concentration:

$$\mathrm{G}^{P}_{i\sim j,n}=\left(\sum_{l=i}^{j}u_{l,n}P_l\right)\Big/\left(\sum_{l=i}^{j}u_{ref,l,n}P_l\right), \tag{15b}$$

and square root pressure-weighted gas concentration:

$$\mathrm{G}^{\sqrt{P}}_{i\sim j,n}=\left(\sum_{l=i}^{j}u_{l,n}\sqrt{P_l}\right)\Big/\left(\sum_{l=i}^{j}u_{ref,l,n}\sqrt{P_l}\right). \tag{15c}$$

We compute $\mathrm{G}_{i\sim j,n}$ and $\overline{\tau}_{r,i\sim j,n}$ for various spectral bands with an atmospheric profile dataset used in [14]. The profiles cover varied atmospheric conditions on the earth. Figure 1 shows two $\mathrm{G}_{i\sim j,n}\sim\overline{\tau}_{r,i\sim j,n}$ relations for O_3 in MODIS band 30. The SRFs of MODIS bands are obtained from the website [85]. For O_3 at band 30, the square root pressure-weighted gas concentration has the smoothest $\mathrm{G}_{i\sim j,n}\sim\overline{\tau}_{r,i\sim j,n}$ relation. If the $\mathrm{G}_{i\sim j,n}\sim\overline{\tau}_{r,i\sim j,n}$ relation is smooth, the polynomial parameterization should be accurate. The form of $\mathrm{G}_{i\sim j,n}$ that has the smallest polynomial fitting error is selected for each specific gas in a band.

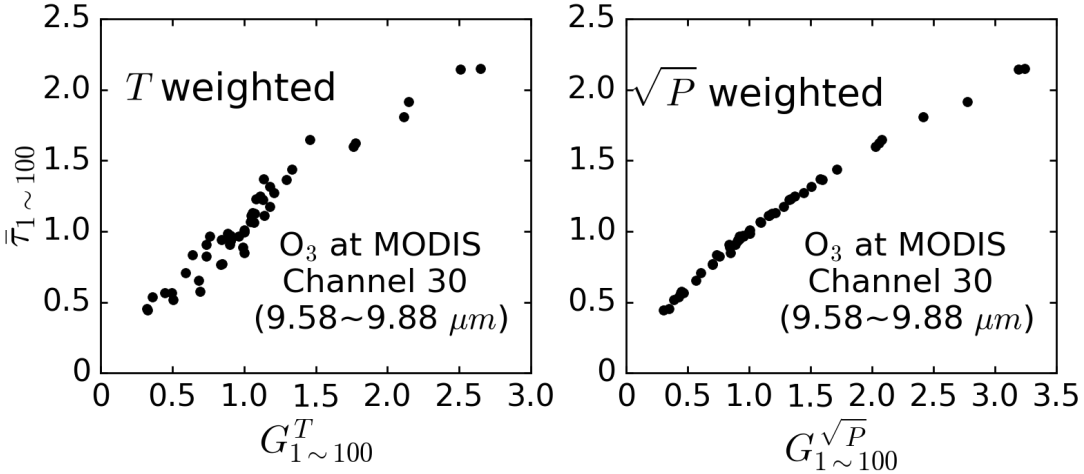

Figure 1. Relative CAOT of O_3 in all model pressure layers versus two gas concentration predictors in MODIS Channel 30. **Left:** Temperature-weighted; **Right:** Square root-pressure weighted.

The exponent γ in Eq. (13) is also determined by a trial-and-error approach to obtain the smallest fitting error. The variation of γ is due to different relations between CAOT and gas concentration. The spectral transmittance in Goody's statistical band model [30] can be written as

$$\overline{t} = \exp\left[-\frac{uA_m\alpha}{\Delta\upsilon\sqrt{\alpha^2 + \frac{uA_m\alpha}{\pi}}}\right], \tag{16}$$

where $\Delta\upsilon$ is the mean absorption line spacing, α the absorption line width, and A_m the mean absorption line intensity. From the definition of CAOT in Eqs. (8) and (16), the CAOT is proportional to u^γ in the statistical band model. Because A_m and α are not constant, γ varies in the band model. Although the Goody's statistical band model is an approximation, it shows the rationale of including the exponent γ in the gas concentration predictors.

Many channels are associated with absorption by more than one absorptive gas. According to Eq. (9), except for gas *N*, the CAOT of an absorptive gas depends on the CAOTs of other gases with larger indices. For example, $\overline{\tau}_{i\sim j,n}$ is dependent on the CAOTs of gases 2~*N*. To simplify the parameterization of CAOT, the CAOT interdependence is neglected in the channels where one gas is much more absorptive than others. The most strongly absorptive gas is assigned to be gas *N*. Its CAOT is computed by Eq. (7). In most of the channels in the UV-IR band, only one gas dominates absorption. There are a few channels in the IR band where CO_2 and other gases dominate absorption. Because the CO_2 concentration variation is small, we choose CO_2 as gas *N* in these channels. The CAOTs of other gases are affected by the CO_2 concentration. We thus add an extra CO_2 predictor term in Eq. (13),

$$\overline{\tau}_{r,i\sim j,n} = \sum_{k=1}^{K}\sum_{h=0}^{H} c_{kh}\left(\mathrm{G}_{i\sim j,n}^{\gamma}\right)^k\left(\mathrm{T}_{i\sim j}\right)^h + \mathrm{G}_{i\sim j,\mathrm{CO}_2}\sum_{h=0}^{H} c_{h,\mathrm{CO}_2}\left(\mathrm{T}_{i\sim j}\right)^h, \tag{17}$$

in which $\mathrm{G}_{i\sim j,\mathrm{CO}_2}$ is the predictor for CO_2.

If the polynomial coefficients in Eqs. (13) or (17) are known for a channel, for a specific atmospheric profile, we can first compute predictors $\mathrm{G}_{i\sim j,n}$, and then use Eqs. (13) or (17) to compute CAOTs of the atmosphere for the channel. The polynomial coefficients are determined by a regression approach. The training atmospheric profile dataset is the one used in [14] containing 48 atmospheric profiles under various atmospheric conditions. The regression can be described by a matrix equation,

$$\mathbf{GC} = \mathbf{O}, \tag{18}$$

in which **G** is the predictor matrix, **C** the regression coefficient vector, and **O** the relative CAOT vector.

Using singular value decomposition (SVD), **G** can be decomposed to

$$\mathbf{G} = \mathbf{V}_1\mathbf{\Sigma}\mathbf{V}_2^{\mathrm{T}}, \tag{19}$$

in which $\mathbf{V}_1$ and $\mathbf{V}_2$ are orthogonal matrices, and $\mathbf{\Sigma}$ is a diagonal matrix. Substituting Eq. (19) into Eq. (18), the regression coefficient vector is obtained by

$$\mathbf{C} = \mathbf{V}_1^{\mathrm{T}}\mathbf{\Sigma}^{-1}\mathbf{V}_2\mathbf{O}. \tag{20}$$

For a given atmospheric profile, radiative transfer calculations are usually implemented in multiple viewing geometries, so CATs are needed in different zenith angles. The secant of zenith angle *a* is a variable in Eq. (7), but *a* can be a regression variable, which however, makes regression inaccurate according to our tests. Instead, *a* is set to be a constant in regression. The regressions are performed with 7 secants of zenith angles (1, 1.1, 1.5, 2.0, 3.0, 5.0, and 10.0) respectively, which correspond to zenith angles from 0 to over 84°, and cover the applicable solar and viewing zenith angle ranges in remote sensing. To compute the total CAOT at an arbitrary zenith angle, first, the CAOTs of all absorptive gases are computed at the two *a* values above and below the desired *a* value. Then, the total CAOT at the desired zenith angle is obtained by linear or spline interpolations. The total CAOT is a smooth function with respect to *a*, though it is not linear. The interpolation errors are comparable to regression errors.

Compared with previous regression-based methods, the advantage of the new regression method is that it directly parameterizes the CAOT for an inhomogeneous atmospheric path rather than making parameterizations for each homogeneous layer. This advantage makes the regression approach more efficient, especially for solar band radiative transfer calculations. For example, in Eq. (6a), only the surface-to-TOA CAT is needed so only one calculation is needed to compute the surface-to-TOA CAT by the new regression method in the study. However, previous regression-based methods have to do computations for each layer and then combine the results to obtain the surface-to-TOA CAT. In other words, the speed of the new regression method is independent of the number of layers. In thermal IR (TIR) bands, all of the layer-to-TOA CATs are needed so the speed of the new regression method is not significantly faster.

Because the developed regression-based method relates atmospheric variables to the CAT through polynomials, analytical Jacobian matrix expressions can be easily derived to facilitate retrieval algorithm development.

3.2 Validation

The regression calculations are performed for all MODIS bands. In Fig. 2, we compute the layer-to-TOA CATs by the regression method, line-by-line method and CKD method for the independent atmospheric profiles from a training database of global profiles [86]. We obtain the temperature profile, H_2O mixing ratio, O_3 mixing ratio, surface pressure, and surface temperature of each atmospheric profile from the database. Global mean mixing ratios for other gases are used in the computation. We randomly select 50 clear-sky profiles from the database and compute the layer-to-TOA CATs for zenith angle zero. The layer-to-TOA CATs are used in Eq. (6b) to compute the brightness temperature (BT) at the TOA. The CKD implementation here is similar to [20] and uses 64 integration points. Figure 2 shows the comparisons of BTs at the TOA in 16 MODIS TIR bands computed by the three methods. In terms of root-mean-square error (RMSE) relative to LBLRTM, the regression method performs more accurately than the 64-point CKD method. In band 25, the CKD has a large RMSE. Seven gases are absorptive in band 25. The absorption line overlapping may cause extra errors in the CKD method. In terms of implementation speed, the regression method is four orders of magnitude faster than the line-by-line method. It is also twice as fast as the 64-point CKD method.

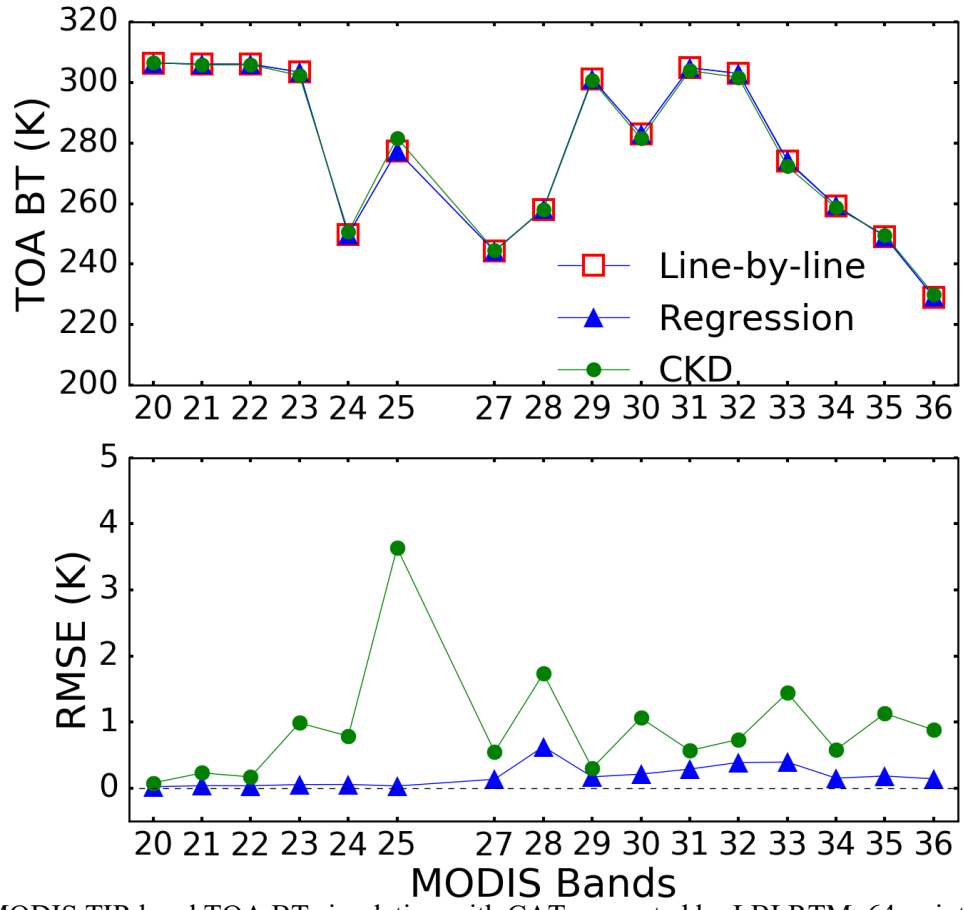

Figure 2. MODIS TIR band TOA BT simulation with CAT computed by LBLRTM, 64-point CKD, and the proposed regression method. The bottom row shows the RMSE of BT compared to LBLRTM.

4. Two-component Method in Multiple Scattering Calculation

4.1 Methodology

The two-component method (referred to as SAA+AD) combines the improved SAA scheme [78] and the AD method [60]. According to [78], the vector RTE Eq. (1) can be split into two decoupled equations,

$$
\begin{aligned}
& u\frac{\partial \mathbf{I}^d\left(\tau_s,u,\varphi\right)}{\partial \tau_s}= \\
& \mathbf{I}^d-\frac{\varpi_s(\tau_s)}{4\pi}\int_{-1}^{1}du'\int_0^{2\pi}d\varphi'\mathbf{P}^d\left(\tau_s,u,u',\varphi-\varphi'\right)\mathbf{I}^d\left(\tau_s,u',\varphi'\right) \\
& -\frac{F_0\varpi_s(\tau_s)}{4\pi}\mathbf{P}^d\left(\tau_s,u,\mu_0,\varphi-\varphi_0\right)\begin{pmatrix}1&0&0&0\end{pmatrix}^{\mathrm{T}}e^{-\frac{\tau}{\mu_0}} \\
& -\left[1-\varpi_s(\tau_s)\right]\mathbf{B}\left[T(\tau_s)\right],
\end{aligned}
\tag{21}
$$

and

$$u\frac{\partial \mathbf{I}^f(\tau,u,\varphi)}{\partial \tau}=\mathbf{I}^f(\tau,u,\varphi)$$
$$-\frac{f_1\varpi(\tau)}{4\pi}\int_{-1}^{1}du'\int_0^{2\pi}d\varphi'\mathbf{P}^f(\tau,u,u',\varphi-\varphi')\mathbf{I}^f(\tau,u',\varphi'). \quad (22)$$

where Eq. (21) is the diffuse RTE, and Eq. (22) is the forward RTE. The quantities with superscripts "*f*" and "*d*" represent "forward" and "diffuse", respectively. f_1 represents the proportion of total scattering energy that is in the forward scattering directions. f_1 is defined as

$$f_1=\frac{1}{2}\int_0^{\Theta_t}a_1(\tau,\Theta)\left[1-\exp\left(-\zeta\frac{\cos\Theta-\cos\Theta_t}{1-\cos\Theta_t}\right)\right]\sin\Theta\,d\Theta. \quad (23)$$

where $a_1(\tau,\Theta)$ is the scattering phase function, Θ_t is the truncation angle, and ζ is an empirical parameter [78]. τ_s is equal to $(1-f_1\varpi)\tau$, and ϖ_s is equal to $(1-f_1)\varpi/(1-f_1\varpi)$.

Sun et al. [78] uses the SAA and SOS methods to solve the forward and diffuse RTEs. In this study, we use SAA to solve Eq. (22) and use the AD method to solve Eq. (21). Sun et al. [78] only considers a single-layer case. Here we further extend the SAA method to a multi-layer case so that it can be applied to multiple inhomogeneous layers including atmosphere and ocean.

Using the SAA, the scalar solution to Eq. (22) is approximated by a 2-dimensional Gaussian function,

$$I^f(\tau,-\mu,\varphi)\approx\frac{1}{2\pi}\frac{F}{\sqrt{V_{nx}V_{ny}}}\exp\left(-\frac{n_x^2}{2V_{nx}}-\frac{n_y^2}{2V_{ny}}\right), \quad (24)$$

where F, V_{nx}, and V_{ny} are parameters determined by the scattering media properties, and n_x and n_y are direction parameters. The detailed derivations of F, V_{nx}, and V_{ny} for an inhomogeneous atmosphere are given in [87]. Note that the energy of the forward solution Eq. (24) is concentrating on several degrees of forward scattering around the incident direction, and its contribution to reflection is negligible, since the forward scattering contribution to the reflection has been included in the decoupled diffuse RTE Eq. (22). Thus, for convenience, the non-negative variable μ instead of u is used to denote zenith directions of the forward solution Eq. (24).

The polarization of the forward solution is approximated by first and second order scattering events, for which exact analytical solutions exist. In the forward component RTE, the forward scattering phase matrix elements are nonzero only in several degrees in the forward scattering directions. During this scattering angle range, the off-diagonal elements are almost zero, and the diagonal elements are almost identical. The polarization contribution by the forward solution is much smaller than the diffuse solution. Thus, we ignore the polarizations of higher order scatterings in the forward solution. Hovenier et al. [50] also shows that polarization calculations converge faster in terms of scattering orders than radiance.

The SAA solution, Eq. (24), as an approximation, is the sum of all orders of scattering. To improve the accuracy of the forward solution, we replace the first and second orders of scattering components in Eq. (24) with the accurate counterparts [78]. The explicit expressions of the first and second orders of scattering solutions can be found in [50].

The diffuse RTE Eq. (21) is equivalent to a scaled RTE based on the similarity relation [88]. DMM and DFM truncation methods give the same forms of scaled RTE as Eq. (21) but the definitions of f_1 and $\mathbf{P}^d$ are different. The definitions of f_1 and $\mathbf{P}^d$ in DMM and DFM are given in [63-64, 68]. Equation (21) is solved by the AD method. The sum of forward and diffuse RTE solutions is approximately equal to the solution to the vector RTE Eq. (1).

4.2 Validation

To validate the two-component method, we first compare its computation results with a published dataset by Kokhanovsky et al. [89]. They use several numerically accurate vector RTE solvers to compute the reflected and transmitted Stokes vectors by a liquid cloud and an aerosol layer at wavelength 0.412 μm. The cloud and aerosol single-scattering properties are computed by the Lorenz-Mie theory. Two size distributions are used to obtain the size-averaged scattering matrices of the cloud and aerosol models. We also include comparisons with the VLIDORT model developed by Spurr [57] and adding-doubling with DFM and TMS single-scattering correction (DFM&TMS+AD) [68]. The VLIDORT uses the DO method to solve the vector RTE. The VLIDORT calculations incorporate the DMM and TMS single-scattering correction. The comparisons focus on the radiance I and the degree of linear polarization (DoLP) defined as $\sqrt{Q^2+U^2}/I$, in which Q and U are Stokes parameters representing linear polarization.

Figures 3 and 4 show the SAA+AD, VLIDORT and DFM&TMS+AD multiple scattering computations compared with the published results in [89]. The RT calculation in a retrieval algorithm must have errors smaller than the remote sensing measurement error. For example, the Ocean Color Instrument for PACE mission is expected to have systematic error less than 0.5% at the TOA [90]. The SPEXone polarimeter is expected to have DoLP accuracy as high as 0.003 and radiometric systematic error less than 2% [91]. We perform the RT calculations to obtain the results with certain accuracy and compare the computational speeds.

Figure 3 shows the radiance and DoLP of the transmitted radiation in the case of an aerosol layer. The aerosol layer has optical thickness 0.3262 and is assumed to be nonabsorptive. In the transmission case (Fig. 3), the relative azimuth angle is 0°. The DoLP results of the three methods all have accuracy less than 0.001. The SAA+AD radiance result has percentage error less than 2% in all viewing zenith angles in transmission direction. The VLIDORT and DFM&TMS+AD method radiance errors are also less than 2% except for around the forward scattering direction, which has viewing zenith angle 120°. As stated in Section 2, TMS single-scattering correction introduces an extra source term in the forward scattering direction [68], which overestimates the result in the forward direction. In the SAA+AD method, the forward scattering is analytically computed based on two approximations. One is, in the SAA, the angular distribution of the forward radiance is approximated by a Gaussian distribution [78]. Another is, the polarization contribution of the forward solution is approximated by first and second order scatterings. In terms of speed, the SAA+AD and VLIDORT are similar, and DFM&TMS+AD is slightly faster.

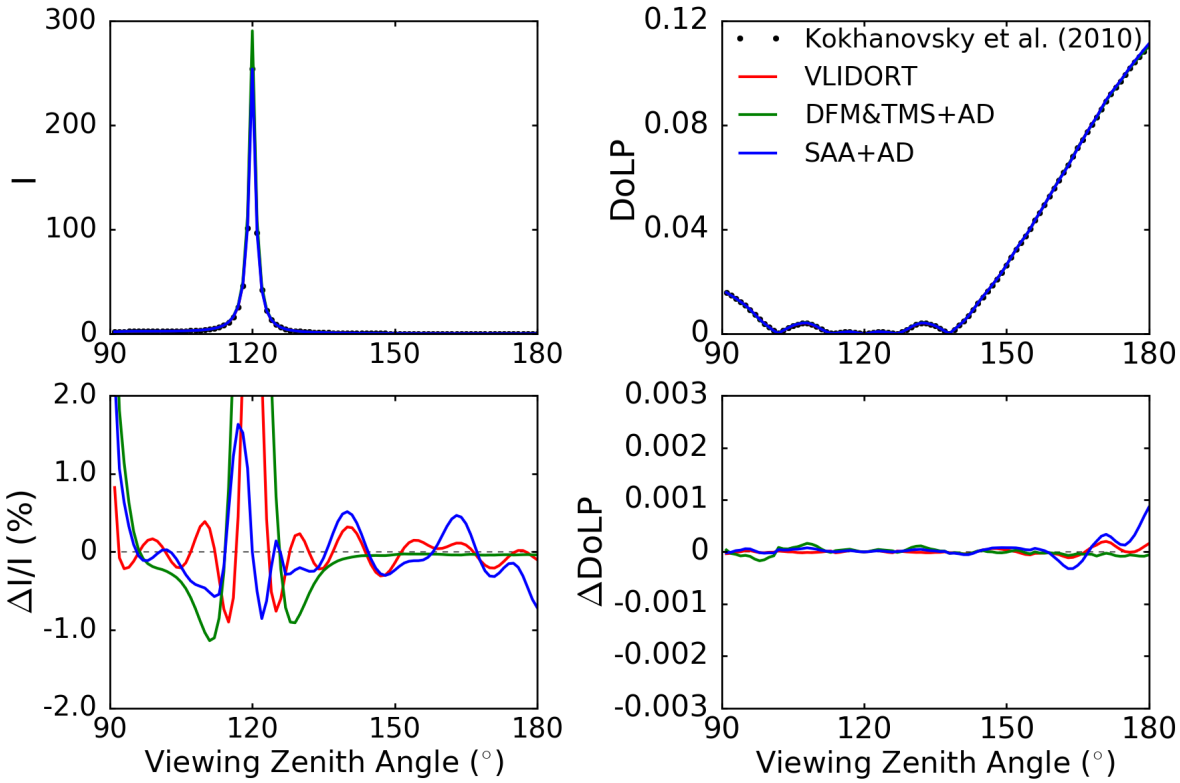

Figure 3. Radiance I and DoLP of the transmitted radiation and the differences in the case of an aerosol layer. The SAA+AD method, VLIDORT and DFM&TMS+AD are used in the calculations. The results are compared with the published results in [89]. The solar zenith angle is 60° and the relative azimuth angle is 0. The aerosol optical thickness is 0.3262. ΔI/I is the relative difference in percentage, and ΔDoLP is absolute differences. The radiances are normalized by the incident radiance so they are dimensionless.

Figure 4 shows the radiance and DoLP of the reflected radiation in the case of a liquid cloud layer. The liquid cloud layer has an optical thickness 5 and is assumed to be nonabsorptive. The relative azimuth angle is 90°. The radiance percentage errors of the three methods are all less than 0.5%, and the DoLP errors are less than 0.001. The SAA+AD method is slightly faster than the VLIDORT, and more than three times faster than the DFM&TMS+AD method, since more GSF expansion terms are needed in the DFM&TMS+AD calculation to satisfy the current accuracy.

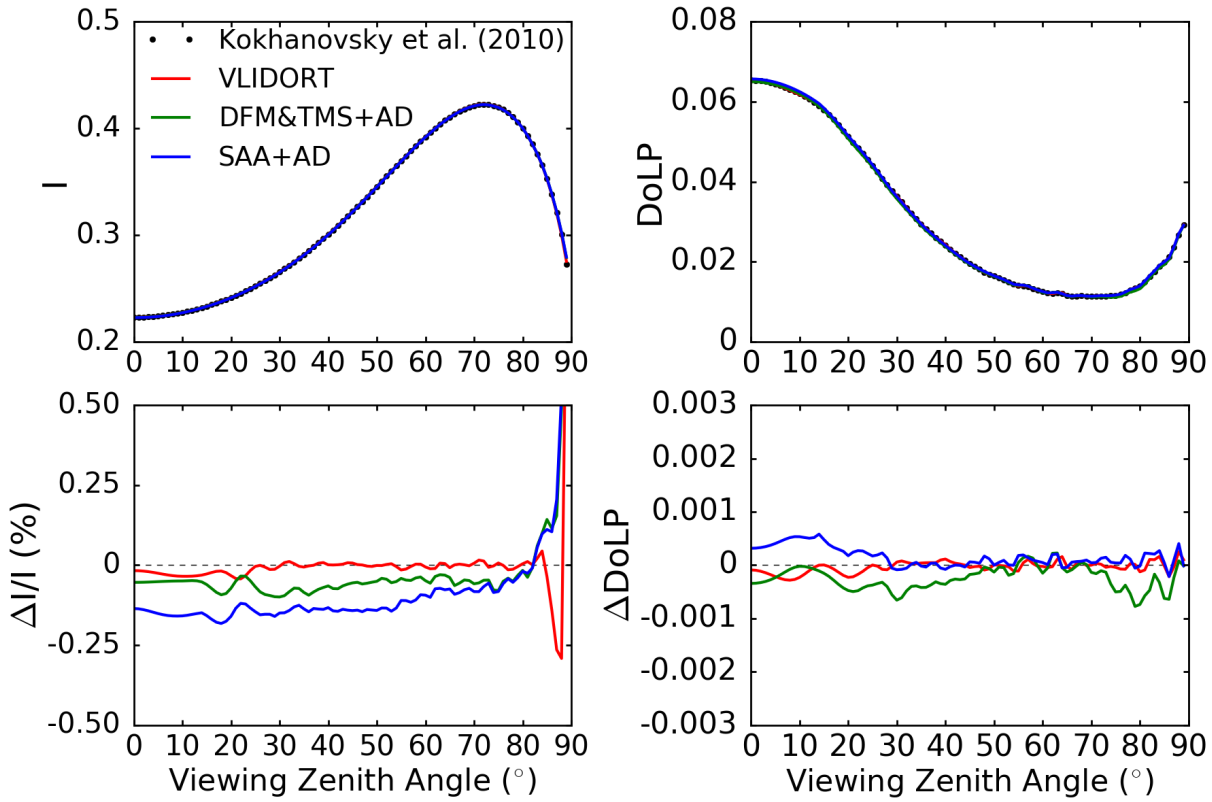

Figure 4. Radiance I and DoLP of the reflected radiation and the differences in the case of a liquid cloud layer. The SAA+AD method, VLIDORT and DFM&TMS+AD are used in the calculations. The results are compared with the published results in [89]. The solar zenith angle is 60° and the relative azimuth angle is 90°. The cloud optical thickness is 5. ΔI/I is the relative difference in percentage, and ΔDoLP is absolute difference. The radiances are normalized by the incident radiance so they are dimensionless.

We also compare the SAA+AD method with VLIDORT and DFM&TMS+AD for an ice cloud layer at wavelength 0.865 μm, where the ice cloud does not absorb radiation. The ice cloud model is the MODIS Collection 6 model [92], which has the particle shape of roughened 8-hexagonal column aggregate defined by Yang et al. [93]. The ice cloud effective radius is 30 μm. Figure 5 shows the radiance and DoLP of the reflected radiation in the case of an ice cloud layer. The ice cloud layer has an optical thickness 5. The relative azimuth angle is 90°. The SAA+AD, VLIDORT and DFM&TMS+AD results are compared with the result by the DMM [63] + AD and the TMS single-scattering correction [69] (DMM&TMS+AD). In the DMM&TMS+AD calculations, the scattering matrices are truncated at the 600th expansion term, which is assumed to be rigorous in the reflected radiation calculation. As shown in Fig. 5, all the three methods are accurate and within the accuracy requirement mentioned above. The three methods have similar computational efficiency in the case of an ice cloud.

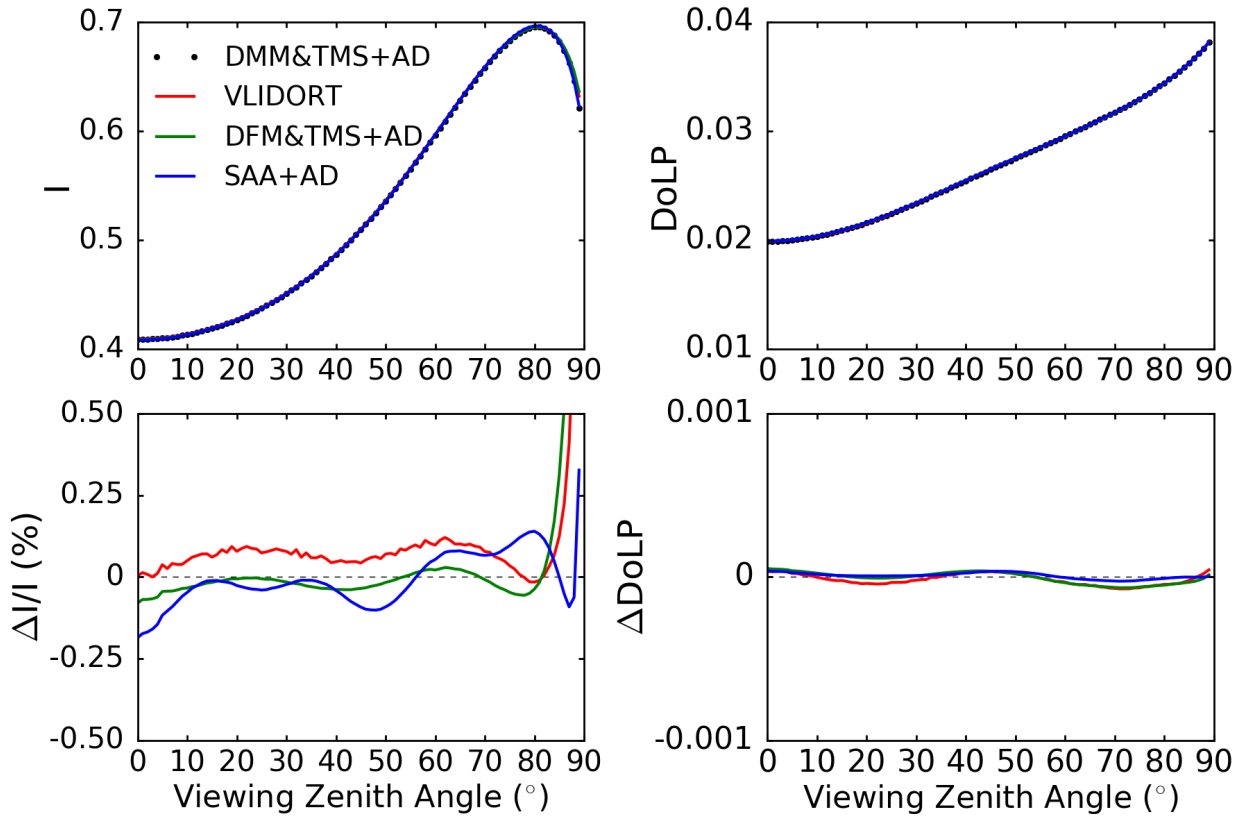

Figure 5. Radiance I and DoLP of the reflected radiation and the differences in the case of an ice cloud layer. The SAA+AD, VLIDORT, DFM&TMS+AD and DMM&TMS+AD are used in the calculations. The solar zenith angle is 60° and the relative azimuth angle is 90°. The ice cloud optical thickness is 5. ΔI/I is the relative difference in percentage, and ΔDoLP is absolute difference. The radiances are normalized by the incident radiance so they are dimensionless.

Next, we validate the two-component vector RTE solver in the case of multiple scattering layers. The model atmosphere has three layers. From the top to bottom, there are an ice cloud layer, an aerosol layer and a liquid cloud layer. The optical thicknesses are 2, 0.3, and 3, respectively. The effective radii are 5, 1.0, and 10 μm, respectively. The surface in the calculation is assumed to be completely absorptive so there is no interaction between the atmosphere and the surface. The wavelength is 0.865 μm. The ice cloud model is the MODIS Collection 6 model. The aerosol layer is assumed to be a dust layer. The dust particle shape is a hexahedron ensemble defined in [94]. The refractive index of dust aerosol is from a compiled dataset [95]. The dust single-scattering properties are computed by a synergistic combination of the invariant imbedding T-matrix (IITM) [96] and physical-geometric optics method (PGOM) [97].

As a benchmark, the rigorous AD method is used to compute the Stokes vector in reflection and transmission directions. In the calculation, the scattering matrices of the scattering layers are expanded in terms of GSF up to 2000 terms, which is accurate enough to represent the scattering matrices. We also perform computation with the DFM&TMS+AD and DMM&TMS+AD, for comparison with the two-component approach. Figures 6 and 7 show the results for the rigorous AD, and the approximate SAA+AD, DFM&TMS+AD and DMM&TMS+AD methods.

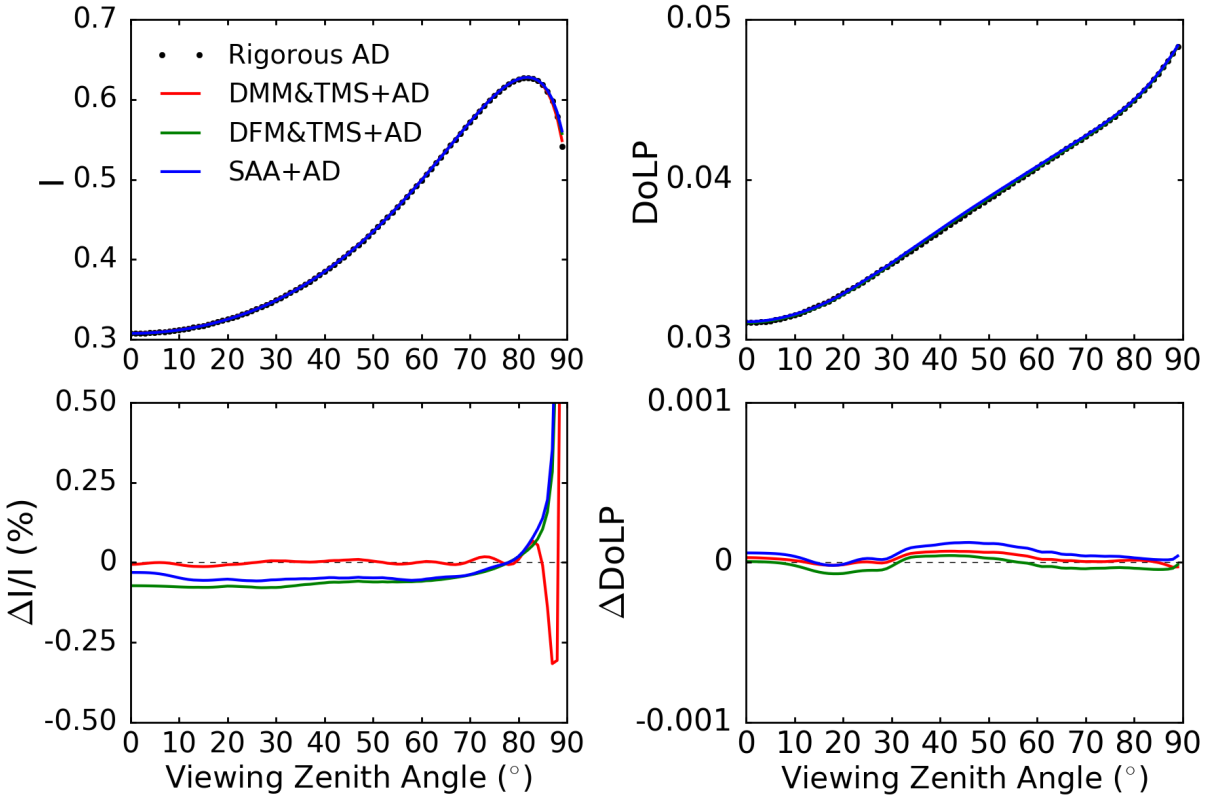

Figure 6. Radiance I and DoLP of reflected radiation computed by the rigorous AD, and the approximate SAA+AD, DFM&TMS+AD and DMM&TMS+AD methods for a three-layer atmosphere (from top to bottom: ice cloud, aerosol, and liquid cloud with optical thickness at 0.865 μm wavelength 2, 0.3, and 3 respectively; and effective radii 5.0, 1.0, and 10 μm respectively). The solar zenith angle is 60°. The relative azimuth angle is 90°. ΔI/I is the relative difference in percentage, and ΔDoLP is absolute difference. The radiances are normalized by the incident radiance so they are dimensionless.

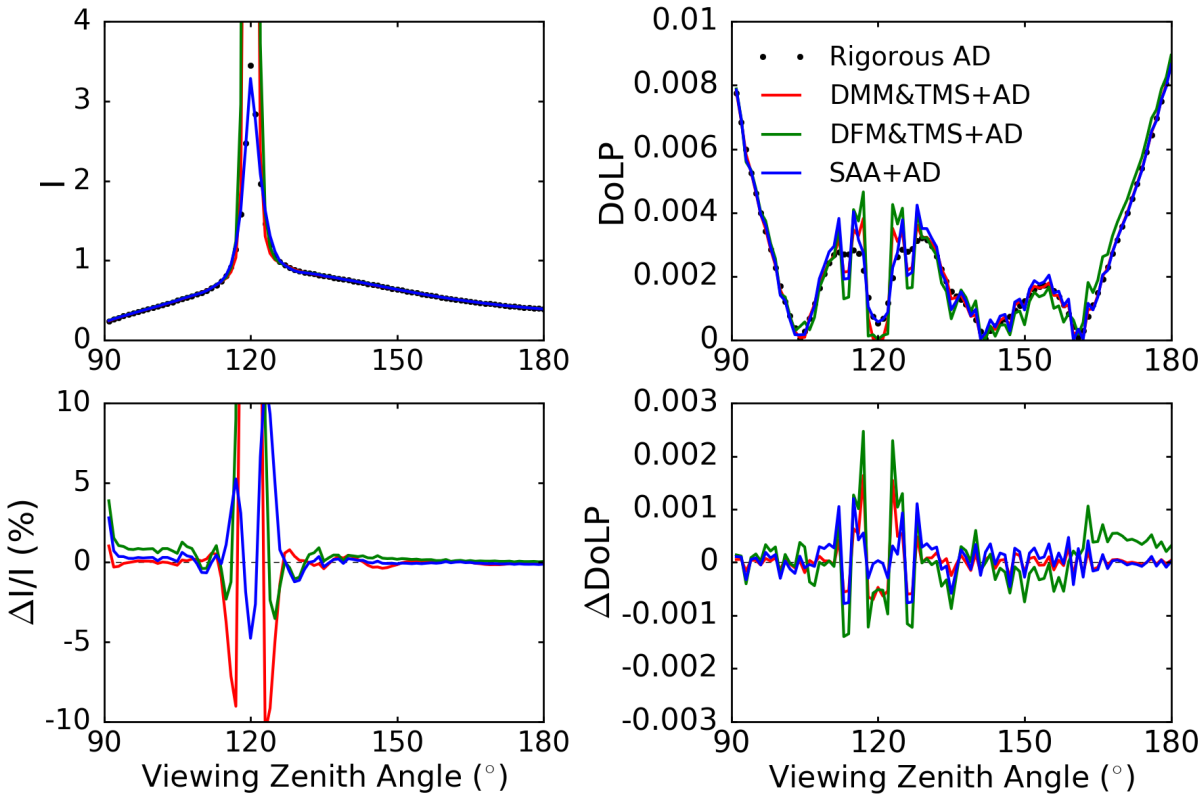

Figure 7. Radiance I and DoLP of transmitted radiation computed by the rigorous AD, and approximate SAA+AD, DFM&TMS+AD and DMM&TMS+AD methods for a three-layer atmosphere (from top to bottom: ice cloud, aerosol, and liquid cloud with optical thickness at 0.865 μm wavelength 2, 0.3, and 3 respectively; and effective radii 5.0, 1.0, and 10 μm respectively). The solar zenith angle is 60°. The relative azimuth angle is 0. ΔI/I is the relative difference in percentage, and ΔDoLP is absolute difference. The radiances are normalized by the incident radiance so they are dimensionless.

In reflection directions as shown in Fig. 6, the SAA+AD, DFM&TMS+AD and DMM&TMS+AD methods are accurate in most directions compared with the rigorous AD. In transmission directions as shown in Fig. 7, the SAA+AD is much more accurate than DMM&TMS+AD in the forward transmitted direction (i.e. viewing zenith angle 120°). The percentage error in the forward direction is less than 10%, which is larger than the percentage error for a thin aerosol layer as shown in Fig. 3. Note that, the total optical thickness of the model atmosphere is 5.3. In Fig. 3, the aerosol layer optical thickness is 0.3262 so the first and second scattering events dominate the signal in the forward direction. For the optical thickness 5.3, there is significant high-order (more than 2) scattering contribution in the forward direction signal.

The forward solution contains all orders of scatterings. In the calculations, the first and second order scatterings are replaced by the accurate solutions as mentioned above. The remaining high order scattering events are less accurate because of SAA. Thus, when the first or second order scatterings dominate the signal, the solution can be accurate. In contrast, when the high order scatterings dominate the signal, the error in the solution is large. Although SAA performs worse with a large optical thickness, there is little effect on a remote sensing application. The forward scattering contribution to the reflected signal is significant only when the atmosphere has small optical thickness where the sky is clear or only a thin aerosol layer exists.

In terms of speed, the SAA+AD method is more than three orders of magnitude faster than the rigorous AD, and about twice faster than the DFM&TMS+AD method since extra more GSF expansion terms are needed in the DFM&TMS+AD calculation to obtain similar accuracy with the SAA+AD method. The SAA+AD method is also slightly faster than the DMM&TMS+AD method.

5. Thermal Emission in Adding-doubling

As in Eq. (2), Eq. (21) can also be written as two decoupled vector RTEs with solar and thermal sources, respectively. In a plane-parallel atmosphere, the radiative transfer of thermal emission by the scattering medium is azimuth-independent. We also assume the terrestrial surface emission and reflection are azimuth-independent for thermal emission radiative transfer. Thus, we only need to consider the azimuth-independent solution, which corresponds to the zero order Fourier expansion term. The azimuth-independent vector RTE is written as

$$u\frac{\partial \mathbf{I}(\tau,u)}{\partial \tau}=\mathbf{I}(\tau,u)-\frac{\varpi(\tau)}{2}\int_{-1}^{1}du'\mathbf{P}(\tau,u,u')\mathbf{I}(\tau,u')-\left[1-\varpi(\tau)\right]\mathbf{B}\left[T(\tau)\right], \qquad (25)$$

where $\mathbf{P}(\tau,u,u')$ is the zero order Fourier component of the phase matrix, and is computed by

$$\mathbf{P}(\tau,u,u')=\frac{1}{2\pi}\int_{0}^{2\pi}\mathbf{P}(\tau,u,u',\varphi-\varphi')d\varphi'. \qquad (26)$$

As shown in the Planck function term in Eq. (25), the thermal emission source is dependent on the temperature. In a planetary atmosphere, although the layer scattering property may be homogeneous, the temperature is hardly constant in the vertical direction. A straightforward idea for solving the vector RTE with thermal emission is to use the adding process.

If a scattering layer has homogeneous scattering properties but the thermal emission is different within the layer due to different temperatures, we cannot implement the doubling calculation, which is more computationally efficient than the adding calculation. Wiscombe [79] shows that if we make some assumptions for the thermal source, the inhomogeneous thermal source can be decomposed into the sum of homogenous components. Here we extend the approach in [79] to consider polarization of thermal emission in a scattering layer.

We have to know the temperatures at all height in the layer to compute thermal emission accurately, which, however, is usually unknown in the real atmosphere. Instead, we assume that layer top and bottom temperatures are known, and the Planck function is linear with optical thickness. The upward and downward thermal emission Stokes vectors for a scattering layer are approximated by

$$\mathbf{I}^{\uparrow}=\frac{1}{2}\left(B_t+B_b\right)\mathbf{Y}+B'\mathbf{Z}, \qquad (27a)$$

$$\mathbf{I}^{\downarrow}=\frac{1}{2}\left(B_t+B_b\right)\mathbf{Y}-B'\mathbf{Z}, \qquad (27b)$$

where **Y** and **Z** vectors are obtained by doubling method. B_t and B_b are Planck functions computed at the layer top and bottom temperatures respectively. B' is equal to $(B_b-B_t)/b$, in which b is the layer optical thickness. The expressions and derivations of **Y** and **Z** vectors are given in [87].

We use the Discrete Ordinate Radiative Transfer (DISORT) model developed by Stamnes et al. [98] to validate the adding-doubling thermal emission calculation approach. In the

validation, the model atmosphere has an ice cloud layer above a Lambertian surface with albedo 0.3. The surface temperature is set to 288 K. The cloud top and bottom temperatures are 255 K and 260 K respectively. The ice cloud has effective radius 30 μm. The MODIS Collection 6 model is used as the ice cloud model. The wavelength is 3.8 μm in the simulation. Figure 8 shows the upward TOA thermal emission simulated by the adding-doubling approach and DISORT. The radiance is converted to brightness temperature in Fig. 8.

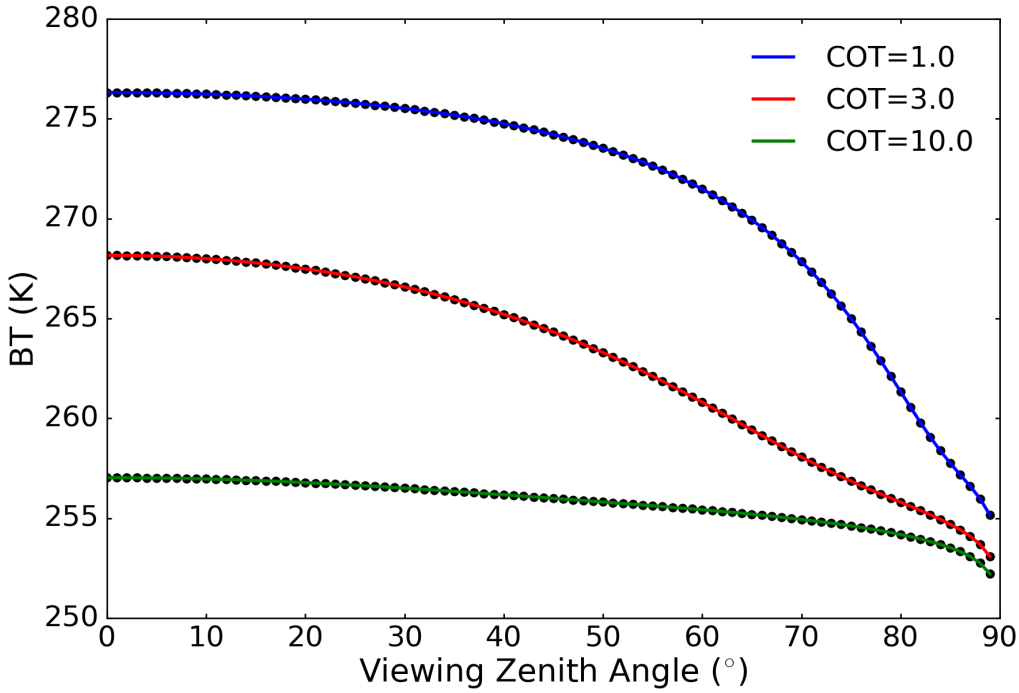

Figure 8. TOA thermal emission at 3.8 μm simulated by adding-doubling and DISORT. The model atmosphere has an ice cloud layer with varied cloud optical thicknesses (COT=1.0, 3.0, or 10.0) and effective radius 30 μm. Cloud top and bottom temperatures are 255 K and 260 K respectively. A Lambertian surface with temperature 288 K and emissivity 0.3 is assumed in the simulation. **Solid lines:** adding-doubling; **Dots:** DISORT.

Three different cloud optical thicknesses (COTs) are assumed in the simulation. The adding-doubling and DISORT results are consistent in all cases to at least four decimal places. As shown in Fig. 8, for larger COT, the TOA BT is smaller, which suggests less thermal emission radiates to the space. Because DISORT is a scalar RTM, polarization is not considered in the validation, although the adding-doubling approach is able to consider the polarization state of thermal emission.

6. Ocean Module

Because the atmosphere and ocean have different refractive indices, radiation traveling through the air-sea interface will experience refraction and reflection. The optical properties of the ocean are determined by the morphology of the ocean surface and the properties of the ocean water. The ocean bottom is assumed to be completely absorptive so there is no reflection by the ocean bottom.

In the model, we assume that the ocean surface is a wind-ruffled rough surface. The surface is a collection of tilted facets with randomly oriented normal directions. The normal directions of the facets follow the Gaussian distribution with the variance as a function of wind speed and direction (i.e. Cox-Munk model) [99]. We incorporate the interface reflection and transmission matrices derived by Zhai et al. [47] in the model. The reflection and transmission matrices are functions of incident and outgoing angles, and ocean surface wind speed and direction. To balance the accuracy and efficiency of RT calculations involving an air-sea interface, we use the following approximation [77],

$$\mathbf{I}_{\text{tot}} = \mathbf{I}_{\text{tot,1D}} - \mathbf{I}_{\text{dir,1D}} + \mathbf{I}_{\text{dir,2D}}, \tag{28}$$

where $\mathbf{I}_{\text{tot}}$ is the output Stokes vector, $\mathbf{I}_{\text{tot,1D}}$ includes all orders of scattering assuming the air-sea interface is one-dimensional (1-D) and independent of wind direction, $\mathbf{I}_{\text{dir,1D}}$ accounts for direct incident solar beam reflected by and transmitting the 1-D air-sea interface, and $\mathbf{I}_{\text{dir,2D}}$ is the 2-D counterpart of $\mathbf{I}_{\text{dir,1D}}$ and is dependent on wind direction. The approximation Eq. (28) is shown to be able to accurately simulate sun glint phenomenon [77], since the direct incident solar beam reflection accounts for a large amount of sun glint signal.

In nature, the composition of ocean water is very complicated and varies spatially and temporally. In the ocean model, the ocean water contains pure water, phytoplankton pigments, CDOM and NAP. The IOPs that are significant in ocean optics and remote sensing include spectral scattering and absorption coefficients, and the Mueller matrix. In our RT calculation, the needed input parameters are optical thickness, single-scattering albedo and scattering matrix. The IOPs can be converted to the RTM input parameters using proper assumptions.

We assume that the IOPs of ocean water are the sums of the corresponding properties of individual oceanic components. For Case I water defined in [100], the total absorption coefficient a_{tot} is

$$a_{\text{tot}} = a_{\text{w}} + a_{\text{c}} + a_{\text{p}}, \tag{29}$$

where the subscripts "w", "c", and "p" represent water, CDOM, and phytoplankton with associated NAPs respectively. Similarly, the total scattering coefficient b_{tot} is

$$b_{\text{tot}} = b_{\text{w}} + b_{\text{p}}, \tag{30}$$

in which the scattering by CDOM is neglected.

The optical thickness of oceanic water is

$$\tau_{\text{o}} = \left(a_{\text{tot}} + b_{\text{tot}}\right) l_{\text{o}}, \tag{31}$$

in which l_{o} is the geometric depth of the ocean. In Eq. (31), the absorption and scattering coefficients are assumed to be constant with depth in the vertical direction. The single-scattering albedo of oceanic water is

$$\varpi_{\text{o}} = \frac{b_{\text{tot}}}{a_{\text{tot}} + b_{\text{tot}}}. \tag{32}$$

The scattering matrix of oceanic water is

$$\mathbf{P}_{\text{o}} = \frac{b_{\text{w}}\mathbf{P}_{\text{w}} + b_{\text{p}}\mathbf{P}_{\text{p}}}{b_{\text{tot}}}. \tag{33}$$

The absorption and scattering coefficients of the ocean water compositions are functions of the compound concentrations as well as wavelength. Previous studies (e.g., [101-106]) measure and analyze the relation between the IOPs and phytoplankton concentration. Here the bio-optical models in the previous studies are adopted in the ocean water model.

For the CDOM absorption coefficient, the wavelength dependence relation of the absorption coefficient proposed by Bricaud et al. [102-103] is used. The spectral pure water absorption coefficient $a_{\mathrm{w}}(\lambda)$ is from the measurement by Pope and Fry [107]. The spectral phytoplankton and associated NAPs absorption coefficients $a_{\mathrm{p}}(\lambda)$ parameterized by Bricaud et al. [101] are considered in the model. The spectral water scattering coefficient b_{w} is obtained by an analytical equation described in [108]. The scattering coefficient of phytoplankton and associated NAPs b_{p} is given by the bio-optical model proposed by Huot et al. [106].

The scattering properties of pure water can be described by Rayleigh scattering theory. We use the Rayleigh scattering phase matrix as pure water phase matrix $\mathbf{P}_{\mathrm{w}}$ and consider the depolarization effect [50]. For the phase matrix of phytoplankton and associated NAPs $\mathbf{P}_{\mathrm{p}}$, we use the distorted hexahedron ensemble model proposed by Xu et al. [109]. The single-scattering properties of the model are computed by a synergistic combination of the IITM method and the PGOM method. The relative refractive indices used in the model development cover the range of aquatic particles [110-111].

In Case II water as defined by Morel and Prieur [100], inorganic particles have a higher concentration than organic particles such as phytoplankton; as a result, inorganic particles dominate the IOP of the ocean water [112]. The organic particles have smaller relative refractive indices than inorganic particles [111]. In Case II water, the bio-optical model introduced above may not be valid.

A distinct feature of the atmosphere-ocean coupled RTM is that it includes both the reflection and transmission matrices of the interface. Figure 9 shows the simulated Stokes vectors of upward radiation immediately above the air-sea interface when the atmosphere is neglected.

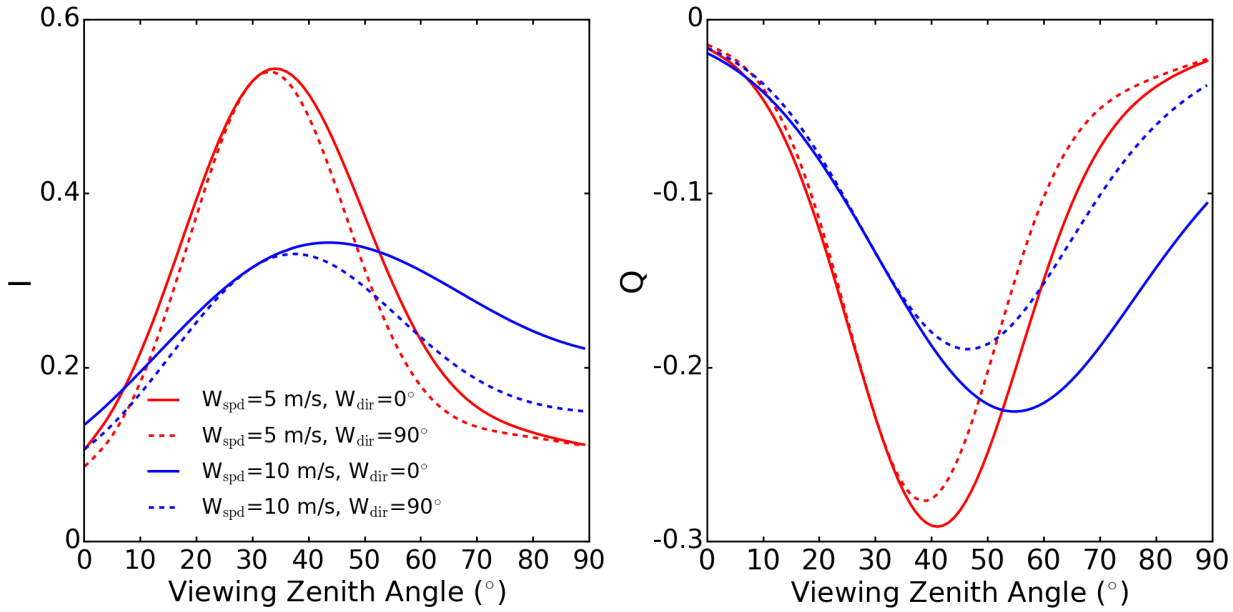

Figure 9. The Stokes vectors of upward radiation computed immediately above the air-sea interface with four different surface wind specified by wind speed (W_{spd}) and direction (W_{dir}). The wind direction is specified by the angle relative to the solar azimuth direction. The solar zenith angle is 30°, and the relative azimuth angle is 0°. The ocean is assumed to have chlorophyll concentration 1.2 mg/m^3, and has optical thickness 10. The complex refractive index of the phytoplankton and associated NAPs is set to 1.06+i0.005. The atmosphere optical thickness is zero. The Stokes vectors are normalized by the incident radiation so they are dimensionless.

Four surface wind are considered in the calculations. The upward radiation comes from reflected radiation by the interface, and the radiation transmitted out of the interface. Obviously, the intensity and polarization of the upward radiation are sensitive to the surface wind speed and direction.

The angular distribution of the upward radiance tends to be more isotropic when the wind speed increases. In the rough surface model introduced above, when the wind speed increases, the variance σ^2 of the probability density function of the surface orientation becomes larger so the rough surface orientation distribution is less anisotropic. The radiation coming from different directions have more uniform chances to be reflected and refracted so the radiance angular distribution is more isotropic.

Using the ocean IOP models described above, and Eqs. (29)-(33), we compute the spectral Stokes vectors of the upward radiation immediately above the air-sea interface in a specific viewing direction, as shown in Fig. 10. At the same wavelength, the radiance is larger for higher chlorophyll concentration, and the absolute values of Stokes elements Q, U and V are also larger, since the scattering ability of the ocean water increases. With the same chlorophyll concentration, the radiance and the absolute values of other Stokes elements decrease almost monotonically from 400 nm to 700 nm wavelengths, since oceanic water absorption ability increases. Figure 10 shows that the upward radiation is sensitive to ocean chlorophyll concentration in terms of both intensity and polarization. The sensitivities of the upward radiation to the ocean surface wind and water properties are the physical bases of ocean remote sensing.

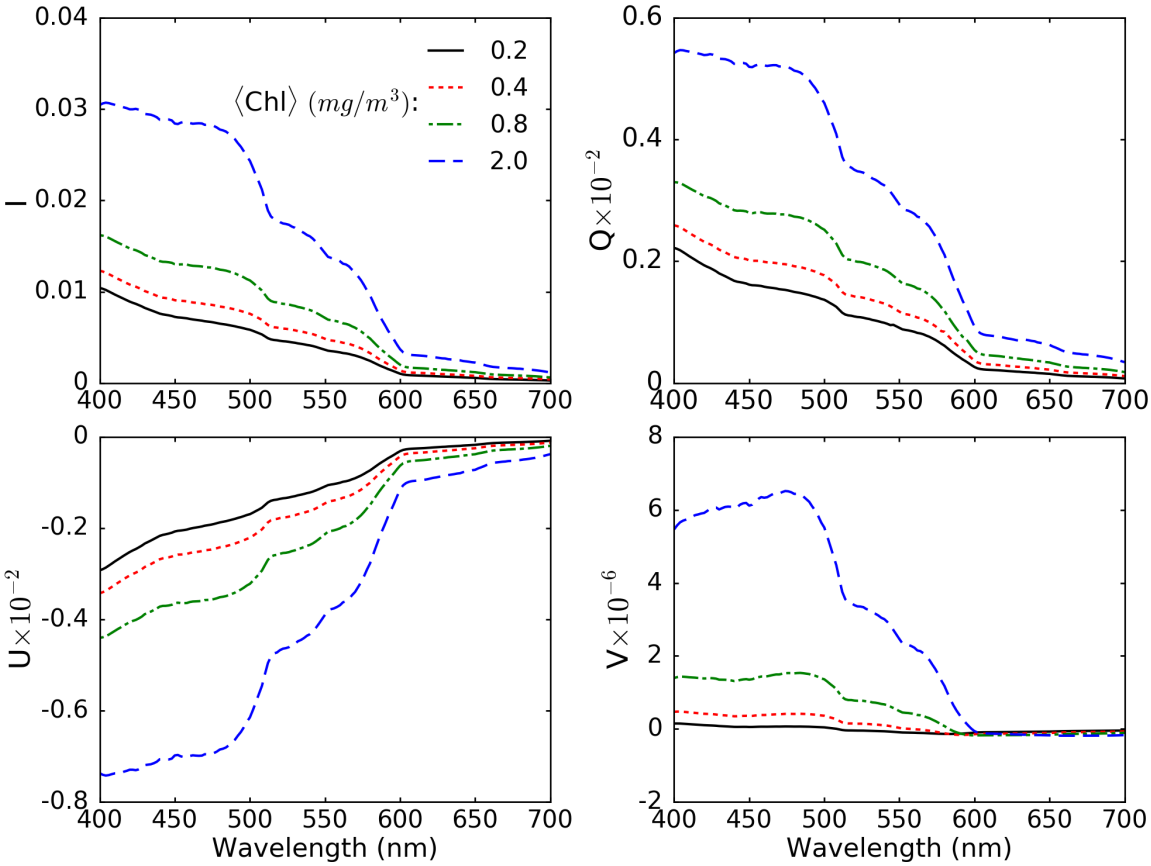

Figure 10. The Stokes vectors of upward radiation computed immediately above the air-sea interface with different chlorophyll concentration $\langle \mathrm{Chl} \rangle$. The surface wind speed is set to be 7 m/s. The wind direction is 120° relative to the solar azimuth direction. The solar zenith angle is 60°, viewing zenith angle is 40°, and the azimuth angle is 90°. The atmosphere optical thickness is zero. The Stokes vectors are normalized by the incident radiation so they are dimensionless.

7. Comparison with Satellite Observations

7.1 Simulation results

All vector RTM modules introduced in previous sections are integrated into a simulator of satellite instruments. In this section, the simulation results are compared with POLDER and MODIS observations. For POLDER observations, the reflectance and polarized reflectance at 0.865 μm band are simulated. For MODIS observations, the radiance at band 31 (10.78~11.28 μm) is simulated.

The simulation region is shown in Fig. 11. The RGB image in Fig. 11 is plotted using reflectance data in 0.490 μm (blue), 0.565 μm (green) and 0.670 μm (red) bands obtained from the Polarization & Anisotropy of Reflectances for Atmospheric Sciences Coupled with Observations from a Lidar (PARASOL) Level-1B product [113], which was derived from the observations of POLDER instrument on board the PARASOL satellite. The region is over the Indian Ocean southwest of Sri Lanka, so no land surface pixels are analyzed in this study. The observation time is 1st July 2008 around 0845 UTC.

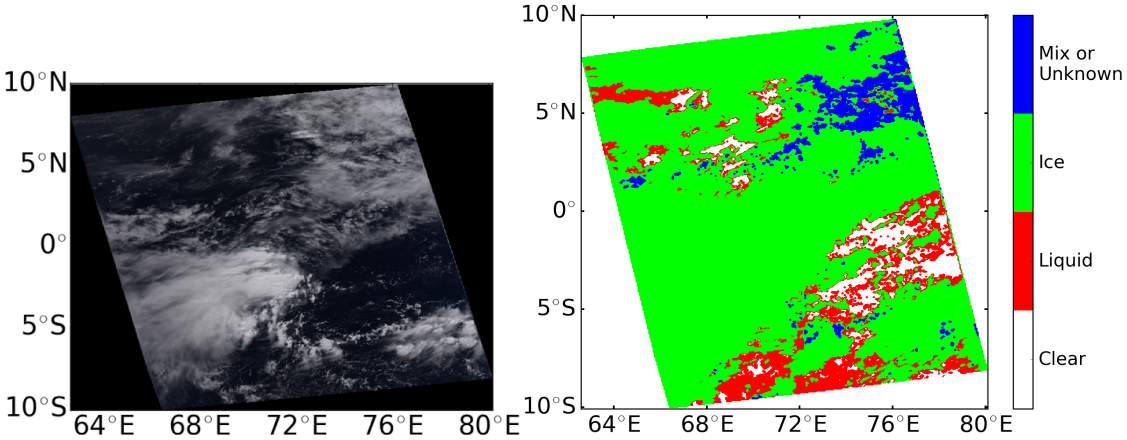

Figure 11. Left: RGB image plotted using the data from PARASOL Level-1B product. The location is over the Indian Ocean southwest of Sri Lanka. The observation time is July 1st, 2008 around 0845 UTC. **Right:** Collocated cloud phase information. The cloud phase data are from Aqua MODIS Level-2 Collection 6 cloud product.

We collocate the PARASOL pixels with the Aqua MODIS Level-2 Collection 6 cloud product [92]. As shown in Fig. 11, many pixels have ice clouds, and other pixels have liquid clouds, clear sky, or mixed phase or unknown clouds.

For the pixels in Fig. 11, we only consider cloudy and clear-sky cases in the simulation and ignore aerosol since aerosol loading is low in this area during the observation period. The cloud phase, cloud optical thickness, cloud effective radius, cloud top height, cloud top pressure, and cloud top temperature are from the collocated Aqua MODIS Level-2 Collection 6 cloud optical property product.

The atmospheric profile data are obtained from collocated Modern-Era Retrospective Analysis for Research and Application, Version 2 (MERRA-2) [114] instantaneous 3h 3-dimensional assimilated meteorological fields, and CO and CO_2 mixing ratios. The ice and liquid cloud models utilized in the simulations are consistent with those used in the MODIS Collection 6 cloud property retrieval algorithm.

Cloud phase data determines the type of cloud model (liquid or ice) to be used in radiative transfer calculations. For a mixed phase or unknown phase, the liquid cloud is assumed in the calculation. The cloud optical thickness is computed at the 0.55 μm wavelength in MODIS data. It can be converted to the optical thickness at another wavelength λ by

$$\tau_{\mathrm{cld}}(\lambda) = \frac{Q_{ext}(\lambda)}{Q_{ext}(0.55)} \tau_{\mathrm{cld}}(0.55), \tag{34}$$

where subscript "cld" denotes cloud. Q_{ext} is the extinction efficiency of the cloud. Because the cloud model single-scattering properties are pre-computed at discrete effective radii, linear interpolations are applied to obtain the cloud scattering matrices at specific effective radii provided by the MODIS cloud effective radius data.

The MODIS cloud top height, pressure and temperature, and MERRA-2 atmospheric profile data are used to determine the above-cloud atmospheric gaseous absorption and Rayleigh scattering. There is no cloud base data available in either dataset. We use the cloud mass fraction information in the MERRA-2 product to estimate the cloud base height, pressure and temperature, which are used to compute the below-cloud atmospheric gaseous absorption and

Rayleigh scattering. The estimated cloud base height and MODIS cloud top height determine the cloud physical thickness. The cloud top and base temperatures are also utilized in cloud thermal emission calculations. The sea surface temperature data in the MERRA-2 product is used to compute ocean surface thermal emission. The sea surface emissivity is set to 0.98 in TIR bands [18].

The gaseous absorption module computes the air absorption optical thickness using MERRA-2 atmospheric profile data. For wavelengths ranging from UV to NIR, the Rayleigh scattering optical thickness by atmospheric gases is comparable to the typical aerosol and thin cirrus cloud optical thickness, and thus should not be ignored in radiative transfer calculations. The Rayleigh optical thickness calculation method and related data in [115] are used to compute air scattering optical thickness and Rayleigh scattering phase matrix.

The total optical thickness and single-scattering albedo in a model atmospheric layer is

$$\tau_a = \tau_{\text{cld}} + \tau_{\text{air}}^{\text{abs}} + \tau_{\text{air}}^{\text{sca}}, \tag{35a}$$

$$\varpi_a = \frac{\tau_{\text{cld}}\varpi_{\text{cld}} + \tau_{\text{air}}^{\text{sca}}}{\tau_a}, \tag{35b}$$

where $\tau_{\text{air}}^{\text{abs}}$ and $\tau_{\text{air}}^{\text{sca}}$ are air absorption and scattering optical thicknesses. The mean phase matrix is

$$\mathbf{P}_a(\Theta) = \frac{\tau_{\text{cld}}\varpi_{\text{cld}}\mathbf{P}_{\text{cld}}(\Theta) + \tau_{\text{air}}^{\text{sca}}\mathbf{P}_{\text{air}}(\Theta)}{\tau_{\text{cld}}\varpi_{\text{cld}} + \tau_{\text{air}}^{\text{sca}}}. \tag{36}$$

The surface wind speed data in the MERRA-2 product are utilized to compute the ocean surface reflection matrix. The wavelengths involved in the simulations are in near-IR bands, where the contribution of water-leaving radiance is very small due to strong absorption by oceanic water. Thus, only the reflection by the ocean surface is considered in the simulations. The layer properties and surface reflection matrix are input to the vector RTE solver that outputs the Stokes vectors at specified positions and directions.

The comparison between the observed and simulated POLDER reflectance is shown in Fig. 12 for the region illustrated in Fig. 11. The simulation looks very similar to the observation, especially in the pixels that have large reflectance. In the pixels that have small reflectance, the difference between the observation and simulation is significant.

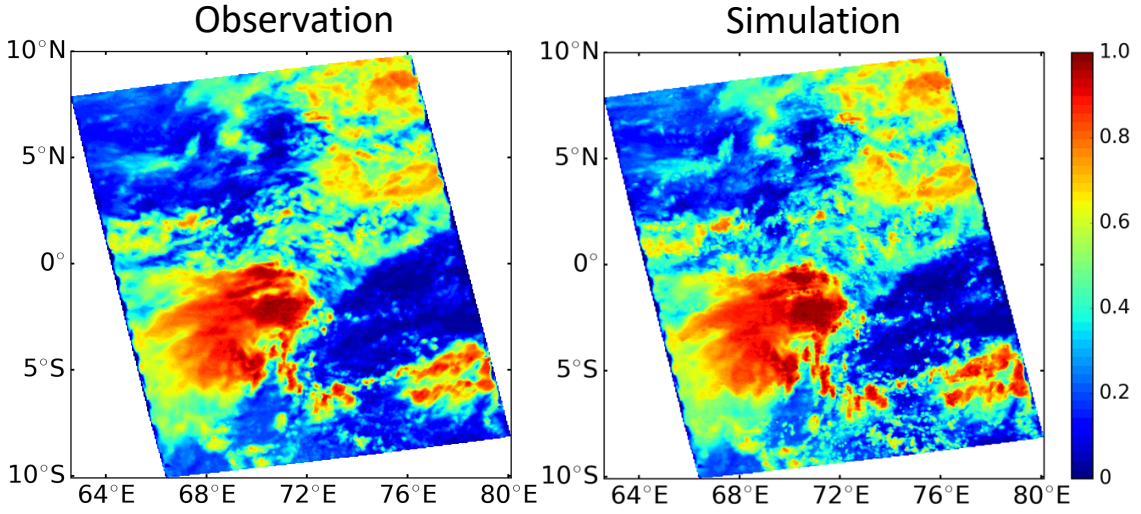

Figure 12. Comparison between the observed (left) and simulated (right) POLDER reflectance at 0.865 μm band for the region in Fig. 11.

Figure 13 shows the observed and simulated POLDER polarized reflectance images. In the lower left part of the images, the polarized reflectance signal is very strong since this part is close to the sun glint area and the clouds are optically thin. In other parts of the two images, it is hardly possible to see the difference. To show other parts clearly, the strong-signal region is set beyond the range of the colorbar. The similarity between the observed and simulated polarized reflectance to some extent shows the accuracy of the developed RTM as well as the polarization consistency of the cloud models used in MODIS retrieval algorithms.

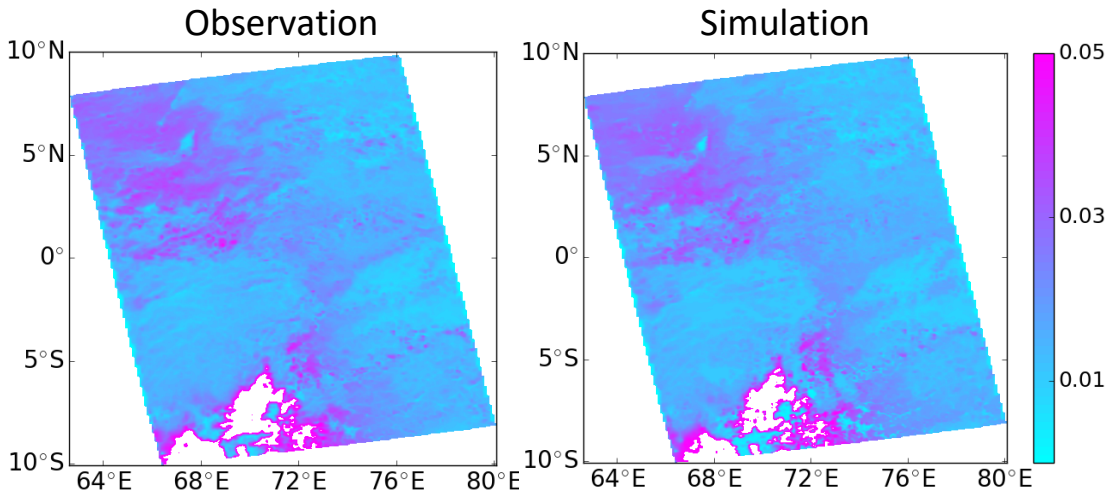

Figure 13. Comparison between the observed (left) and simulated (right) POLDER polarized reflectance in the 0.865 μm band for the region in Fig. 11.

The radiance in MODIS band 31 is the sum of thermal emission by the atmosphere and reflected solar radiation. The solar irradiance F_0 data are obtained from the AER solar irradiance dataset [29]. The Planck function in the simulation is spectrally averaged within the band.

The radiance can be converted to BT by inverting the Planck function at the band central wavenumber. Figure 14 shows the observed and simulated MODIS band 31 radiance in terms of BT. The observation and simulation are similar.

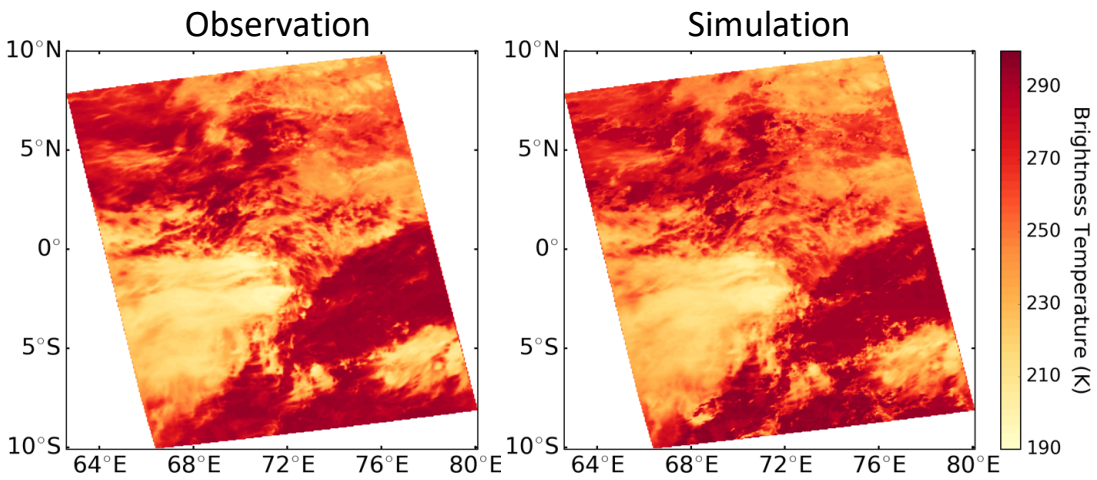

Figure 14. Comparison between the observed (left) and simulated (right) MODIS radiance at band 31 (10.78~11.28 μm) for the region in Fig. 11. The radiance is shown in terms of BT.

The gaseous absorption in MODIS band 31 is weak. The thermal emission from the surface and lower atmosphere can penetrate through the atmosphere and be received by the instrument. If there are clouds, the clouds block the transmission of part of the thermal emission from lower layers, and emit radiation with a colder temperature, which is received by the instrument. Thus, the BT values of cloudy pixels are generally colder than the clear-sky pixels.

We also compute the simulated horizontal minus vertical polarization brightness temperature (BT_H–BT_V) as shown in Fig. 15, with the simulation results in MODIS band 31. The horizontal polarization signal is calculated by I+Q, whereas the vertical polarization signal is calculated by I–Q. I and Q are first two Stokes vector elements. The horizontal and vertical polarization means that the electromagnetic fields are parallel and perpendicular to the plane formed by the local normal direction and the viewing direction, respectively. MODIS does not have polarization capability, so there is no observed MODIS polarization data. Except for the cloud properties, the BT_H–BT_V is also strongly dependent on the viewing zenith angle. Along the satellite track, the viewing zenith angles are close to zero, and the corresponding BT_H–BT_V values are almost zero. For pixels with large viewing zenith angles, the positive BT_H–BT_V values are close to 1 K. The BT_H–BT_V values of optically thick clouds are negative, whereas the BT_H–BT_V values of optically thin clouds are positive. The value of BT_H–BT_V tends to be inversely related to the cloud optical thickness, which is consistent with the POLDER polarized reflectance observations in the 0.865 μm band as shown in Fig. 13.

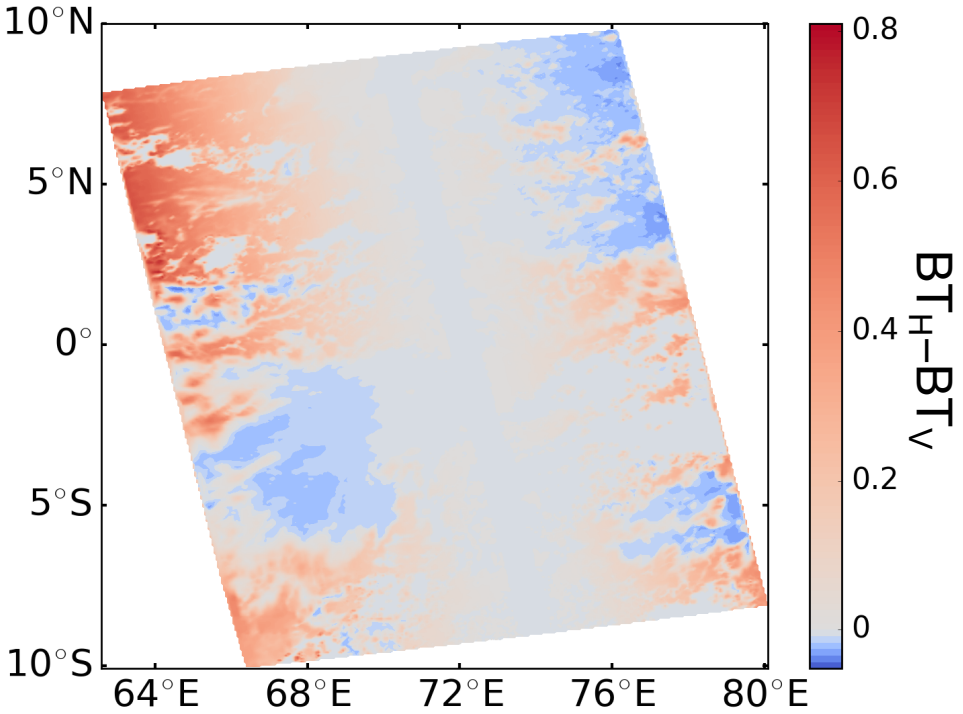

Figure 15. Simulated MODIS band 31 (10.78~11.28 μm) horizontal minus vertical polarization brightness (BT_H–BT_V) for the region in Fig. 11.

7.2 Discussions

The differences between the observations and simulations are attributed to errors in calculation and uncertainties of the input data. The developed RTM is based on the plane-parallel assumption so earth curvature and cloud 3D effects are neglected in the calculation. In addition, all calculations are channel-averaged. Even though the spectral bands considered in the simulation are narrow, the channel-averaged RT calculation still introduces some errors compared with the monochromatic counterpart. These assumptions and approximations affect the accuracy of all computational modules of the model. Each module also has additional local error factors.

In the gaseous absorption calculations, the regression method has regression errors. The atmosphere is divided into a finite number of homogeneous layers. The discretization may introduce some errors. The pressure levels are fixed in the model, and the input atmospheric profiles are interpolated onto the model pressure levels, which adds interpolation errors in the calculation.

In the multiple scattering calculations, the two-component (SAA+AD) method is an approximation so it has errors compared with numerically accurate RTE solvers. Errors also exist in the ocean surface reflectance calculations, because the air-sea interface model is a simple approximation of the complicated real interface.

In the thermal emission calculations, the assumption that the Planck function changes linearly from the cloud base to cloud top may introduce errors, especially for an optically thick cloud. The simulated thermal emissions by optically thick clouds have larger biases than optically thin clouds. The errors in the absorption calculation also propagate into the air thermal emission calculation.

The input cloud properties and atmospheric profiles in the simulations are all obtained from retrievals and reanalysis data. The input data have uncertainties compared with exact atmospheric properties. The atmospheric profile data have lower spatial and temporal resolution than the MODIS and POLDER data. Interpolation is used to obtain atmospheric profiles at each specific pixel location and time. The interpolation error increases the uncertainties of input data.

The comparison between observations and simulations using a single satellite scene may not be sufficient to prove the global accuracy of the developed RTM. It can only show that the RTM can work as a simulator in a retrieval algorithm. The efficiency of implementation is another big concern. The number of pixels in the calculations is over 50,000. The reflectance and polarized reflectance calculations take less than one hour with one core on the TAMU Ada supercomputer. The thermal emission calculation is even faster.

8. Summary

In this study, a fast vector RTM referred to as TAMU-VRTM is developed in support of polarimetric remote sensing of atmospheric and oceanic properties by simulating the remote sensing observation from solar to thermal infrared bands. The TAMU-VRTM can be used as an in-line forward model in a retrieval algorithm to fulfill the accuracy and efficiency requirements of the algorithm implementation. The present model has three main components: a gaseous absorption computational module, a vector RTE solver, and an ocean module.

The gaseous absorption module computes the channel-averaged atmospheric gas transmittance. The gas transmittance is the input to the vector RTE solver. A regression-based method is applied to parameterizing the CAOT versus atmospheric variables such as pressure, temperature and gas concentration, and zenith angle. Compared with traditional regression-based methods that perform regression in each homogeneous layer, the current method takes multiple homogeneous layers as an intact component and only employs a consistent parameterization, which significantly reduces the computational time. The CAOT is found to be a smooth and monotonic function of the weighted sum of gas concentration in different layers. The weights are functions of pressure and temperature. Because a gaseous absorption property depends on gas types and wavelengths, the CAOTs of various gases are parameterized separately in each channel and then added up. The regression equation is constructed as a polynomial function of the weighted sum of the gas concentrations. An LBLRTM is used to compute the CAOTs for each gas in each channel for an atmospheric profile dataset. Then, a numerically stable SVD is applied to solve the regression equations to obtain the regression coefficients. The regression method is implemented in 36 MODIS bands and a hyperspectral spectrum from UV to NIR bands. The RMSE of the transmittance compared with LBLRTM results is as small as 0.005 for most channels. The developed regression method is over 4 orders of magnitude faster than LBLRTM.

The vector RTE solver assumes both an incident solar source and an atmospheric thermal emission source. A two-component (SAA+AD) method is utilized to solve the vector RTE. The anisotropic scattering matrix of atmospheric and oceanic particles is decomposed into forward and diffuse components. The forward component is nonzero only in a small range of angles. The diffuse component is much more isotropic. The Stokes vector of the RTE solution is also expressed as a sum of forward and diffuse components. After some approximations, we obtain decoupled forward and diffuse RTEs. The forward RTE is solved by the SAA method, in which the forward solution is approximated as a two-dimensional Gaussian function. The SAA method in this study is generalized to multi-layer cases so it can be applied to the calculation involving an inhomogeneous medium. The diffuse RTE is solved by the AD method. The forward Stokes

vector computation with SAA is quite fast because the solution is an approximate analytical equation. The AD computation is substantially accelerated due to the fact that the diffuse scattering matrix can be expanded with a much lower order of the GSF. The two-component (SAA+AD) method is more than 3 orders of magnitude faster than the rigorous AD method.

In thermal infrared and microwave bands, thermal emission from the atmosphere and terrestrial surface has a nontrivial contribution to the observed radiation. The thermal emission by the air can be computed if we know the gas transmittances and temperature profiles. Thermal emission by clouds and aerosols experiences multiple scattering. An efficient thermal emission calculation method with multiple scattering is developed based on the AD method. In the RTE with only a thermal emission source, the source function is the Planck function, which is dependent on temperature. In the atmosphere, layer optical properties may be homogeneous, but the vertical temperature varies. The adding process can be used to compute thermal emission by a scattering medium. For a scattering layer with homogeneous optical properties, it is preferable to use the doubling process because it is more efficient than the adding process. In this study, the source function in the RTE is approximated by a linear profile with respect to altitude in a homogenous cloud. The layer top and bottom temperatures are the boundary conditions. Based on this approximation, a doubling process can be utilized to compute the thermal emission by the homogeneous layer, which is much faster than directly adding the inhomogeneous thermal emission from each thin layer.

The ocean module includes an air-sea interface model and an ocean IOP model. A beam incident on the interface experiences reflection and transmission. The reflection and transmission properties of the ocean are determined by the interface morphology and the ocean optical properties. The interface is assumed to be a wind-ruffled rough surface composed of infinite hypothetic small facets. The orientation slopes of the facets follow a 2-dimensional Gaussian distribution whose variance is determined by wind speed, which is consistent with the Cox-Munk model. The reflection and transmission matrices are computed based on the rough interface assumption, and these matrices are directly incorporated into the RTE solver as boundary conditions. The ocean is assumed to be a homogeneous layer in the model. The ocean IOPs include scattering and absorption properties of pure water, phytoplankton, NAP and CDOM. The scattering and absorption coefficients are obtained from measurements and bio-optical models in published studies. The Rayleigh scattering matrix is adopted as the pure water scattering matrix. An ensemble-averaged irregular hexahedron model is assumed to represent phytoplankton and associated NAP shapes to compute a scattering matrix.

As illustrations, the TAMU-VRTM is used to simulate the reflectance and polarized reflectance from POLDER observations, and radiance from MODIS observations. In general, the simulation results are comparable to the observations. The errors in the approximations of the RTM and the uncertainties of the input data can explain the differences between the simulations and observations.

Further development is needed to improve the RTM. Although the RTM is based on a plane-parallel assumption, gaseous absorption calculation could be modified to account for earth curvature without reducing computational speed. For thermal emission calculations in the upper atmosphere, non-LTE radiative transfer can be applied to reduce the error of the current LTE assumption in the upper atmosphere. In addition, the RTM only considers an ice-free ocean as the lower boundary. The RTM should incorporate a land reflection matrix model to be able to do calculations over a land surface with various conditions.

Acknowledgements: This study was supported by a graduate fellowship offered the Hagler Institute for Advanced Study at Texas A&M University (TAMU), by the endowment funds related to the David Bullock Harris Chair in Geosciences at the TAMU College of Geosciences, and partly by NASA Grants NNX15AG66G. Dr. Robert Spurr is thanked for providing the VLIDORT code for comparison with TAMU-VRTM.

References

[1] Mishchenko MI, Travis LD. Satellite retrieval of aerosol properties over the ocean using polarization as well as intensity of reflected sunlight. J Geophys Res 1997;102:16989–7013. doi:10.1029/96JD02425.

[2] Parol F, Buriez JC, Vanbauce C, Riedi J, C.-Labonnote L, Doutriaux-Boucher M, et al. Review of capabilities of multi-angle and polarization cloud measurements from POLDER. Adv Sp Res 2004;33:1080–8. doi:10.1016/S0273-1177(03)00734-8.

[3] Dubovik O, Herman M, Holdak A, Lapyonok T, Tanré D, Deuzé JL, et al. Statistically optimized inversion algorithm for enhanced retrieval of aerosol properties from spectral multi-angle polarimetric satellite observations. Atmos Meas Tech 2011;4:975–1018. doi:10.5194/amt-4-975-2011.

[4] Deschamps PY, Buriez JC, Bréon FM, Leroy M, Podaire A, Bricaud A, et al. The POLDER mission: Instrument characteristics and scientific objectives. IEEE Trans Geosci Remote Sens 1994;32:598–615. doi:10.1109/36.297978.

[5] Diner DJ, Xu F, Garay MJ, Martonchik J V., Rheingans BE, Geier S, et al. The Airborne Multiangle SpectroPolarimetric Imager (AirMSPI): A new tool for aerosol and cloud remote sensing. Atmos Meas Tech 2013;6:2007–25. doi:10.5194/amt-6-2007-2013.

[6] Gong J, Wu DL. Microphysical properties of frozen particles inferred from Global Precipitation Measurement (GPM) Microwave Imager (GMI) polarimetric measurements. Atmos Chem Phys 2017;17:2741–57. doi:10.5194/acp-17-2741-2017.

[7] Gong J, Zeng X, Wu DL, Li X. Diurnal variation of tropical ice cloud microphysics: Evidence from Global Precipitation Measurement Microwave Imager polarimetric measurements. Geophys Res Lett 2018;45:1185–93. doi:10.1002/2017GL075519.

[8] Draper DW, Newell DA, Wentz FJ, Krimchansky S, Skofronick-Jackson GM. The Global Precipitation Measurement (GPM) Microwave Imager (GMI): Instrument overview and early on-orbit performance. IEEE J Sel Top Appl Earth Obs Remote Sens 2015;8:3452–62. doi:10.1109/JSTARS.2015.2403303.

[9] Evans KF, Wang JR, Racette PE, Heymsfield G, Li L. Ice cloud retrievals and analysis with the Compact Scanning Submillimeter Imaging Radiometer and the Cloud Radar System during CRYSTAL FACE. J Appl Meteor 2005;44:839–59. doi:10.1175/JAM2250.1.

[10] Werdell PJ, Behrenfeld MJ, Bontempi PS, Boss E, Cairns B, Davis GT, et al. The Plankton, Aerosol, Cloud, ocean Ecosystem (PACE) mission: Status, science, advances. Bull Am Meteorol Soc 2019:BAMS-D-18-0056.1. doi:10.1175/BAMS-D-18-0056.1.

[11] Liu Y, Diner DJ. Multi-Angle Imager for Aerosols. Public Health Rep 2017;132:14–7. doi:10.1177/0033354916679983.

[12] da Silva A, Swap R, Maring H, Behrenfeld M, Ferrare R, Mace G, et al. ACE 2011-2015 Progress Report and Future Outlook. 2016.

[13] Marbach T, Riedi J, Lacan A, Schlüssel P. The 3MI mission: multi-viewing-channel-polarisation imager of the EUMETSAT polar system: second generation (EPS-SG) dedicated to aerosol and cloud monitoring. In: Shaw JA, LeMaster DA, editors., 2015, p. 961310. doi:10.1117/12.2186978.

[14] Strow LL, Hannon SE, De Souza-Machado S, Motteler HE, Tobin D. An overview of the AIRS radiative transfer model. IEEE Trans Geosci Remote Sens 2003;41:303–13. doi:10.1109/TGRS.2002.808244.

[15] Liu X, Smith WL, Zhou DK, Larar A. Principal component-based radiative transfer model for hyperspectral sensors: theoretical concept. Appl Opt 2006;45:201. doi:10.1364/AO.45.000201.

[16] Moncet J-L, Uymin G, Lipton AE, Snell HE. Infrared radiance modeling by optimal spectral sampling. J Atmos Sci 2008;65:3917–34. doi:10.1175/2008JAS2711.1.

[17] Han Y, van Delst P, Liu Q, Weng F, Yan B, Treadon R, and Derber J: JCSDA community radiative transfer model (CRTM)—version 1, NOAA Tech Rep 2006; 122 pp., NOAA, Washington, D. C. https://repository.library.noaa.gov/view/noaa/1157.

[18] Wang C, Yang P, Liu X. A high-spectral-resolution radiative transfer model for simulating multilayered clouds and aerosols in the infrared spectral region. J Atmos Sci 2015;72:926–42. doi:10.1175/JAS-D-14-0046.1.

[19] Liu X, Yang Q, Li H, Jin Z, Wu W, Kizer S, et al. Development of a fast and accurate PCRTM radiative transfer model in the solar spectral region. Appl Opt 2016;55:8236. doi:10.1364/AO.55.008236.

[20] Liu C, Yang P, Nasiri SL, Platnick S, Meyer KG, Wang C, et al. A fast Visible Infrared Imaging Radiometer Suite simulator for cloudy atmospheres. J Geophys Res 2015;120:240–55. doi:10.1002/2014JD022443.

[21] Kattawar GW, Plass GN, Hitzfelder SJ. Multiple scattered radiation emerging from Rayleigh and continental haze layers 1: Radiance, polarization, and neutral points. Appl Opt 1976;15:632. doi:10.1364/AO.15.000632.

[22] Lacis AA, Chowdhary J, Mishchenko MI, Cairns B. Modeling errors in diffuse-sky radiation: Vector vs scalar treatment. Geophys Res Lett 1998;25:135–8. doi:10.1029/97GL03613.

[23] King MD, Kaufman YJ, Menzel WP, Tanre D. Remote sensing of cloud, aerosol, and water vapor properties from the moderate resolution imaging spectrometer (MODIS). IEEE Trans Geosci Remote Sens 1992;30:2–27. doi:10.1109/36.124212.

[24] Cao C, De Luccia FJ, Xiong X, Wolfe R, Weng F. Early on-orbit performance of the visible infrared imaging radiometer suite onboard the Suomi National Polar-Orbiting Partnership (S-NPP) satellite. IEEE Trans Geosci Remote Sens 2014;52:1142–56. doi:10.1109/TGRS.2013.2247768.

[25] Chowdhary J, Cairns B, Travis LD. Contribution of water-leaving radiances to multiangle, multispectral polarimetric observations over the open ocean: Bio-optical model results for case 1 waters. Appl Opt 2006;45:5542. doi:10.1364/AO.45.005542.

[26] Mishchenko MI, Travis LD, Lacis AA. Multiple Scattering of Light by Particles: Radiative Transfer and Coherent Backscattering. Cambridge: Cambridge University Press; 2006.

[27] Mishchenko MI, Yurkin MA. On the concept of random orientation in far-field electromagnetic scattering by nonspherical particles. Opt Lett 2017;42:494. doi:10.1364/OL.42.000494.

[28] Chen N, Li W, Tanikawa T, Hori M, Shimada R, Aoki T, et al. Fast yet accurate computation of radiances in shortwave infrared satellite remote sensing channels. Opt Express 2017;25:A649. doi:10.1364/OE.25.00A649.

[29] Clough SA, Shephard MW, Mlawer EJ, Delamere JS, Iacono MJ, Cady-Pereira K, et al. Atmospheric radiative transfer modeling: A summary of the AER codes. J Quant Spectrosc Radiat Transfer 2005;91:233–44. doi:10.1016/j.jqsrt.2004.05.058.

[30] Goody RM. A statistical model for water-vapour absorption. Quart J Roy Meteor Soc 1952;78:165–9. doi:10.1002/qj.49707833604.

[31] Goody RM. Discussion of A statistical model for water-vapour absorption. Quart J Roy Meteor Soc 1952;78:165–9. doi:10.1002/qj.49707833604.

[32] Godson WL. The evaluation of infra-red radiative fluxes due to atmospheric water vapour. Quart J Roy Meteor Soc 1953;79:367–79. doi:10.1002/qj.49707934104.

[33] Malkmus W. Random Lorentz band model with exponential-tailed S\^-1 line-intensity distribution function. J Opt Soc Am 1967;57:323–9. doi:10.1364/JOSA.57.000323.

[34] Chou M-D, Arking A. Computation of infrared cooling rates in the water vapor bands. J Atmos Sci 1980;37:855–67. doi:10.1175/1520-0469(1980)037<0855:COICRI>2.0.CO;2.

[35] Bernstein LS, Berk A, Acharya PK, Robertson DC, Anderson GP, Chetwynd JH, et al. Very narrow band model calculations of atmospheric fluxes and cooling rates. J Atmos Sci 1996;53:2887–904. doi:10.1175/1520-0469(1996)053<2887:VNBMCO>2.0.CO;2.

[36] Fu Q, Liou KN. A three-parameter approximation for radiative transfer in nonhomogeneous atmospheres: Application to the O3 9.6-μm band. J Geophys Res 1992;97:13051. doi:10.1029/92JD00999.

[37] Berk A, Conforti P, Kennett R, Perkins T, Hawes F, Berk A, et al. MODTRAN6 : a major upgrade of the MODTRAN radiative transfer code 2014. doi:10.1117/12.2050433.

[38] Lacis AA, Wang W, Hansen JE. Correlated k-distribution method for radiative transfer in climate models: Application to effect of cirrus clouds on climate. NASA. Goddard Sp. Flight Cent. 4th NASA Weather Clim. Progr. Sci. Rev, 1979, p. 309–14.

[39] Goody R, West R, Chen L, Crisp D. The correlated-k method for radiation calculations in nonhomogeneous atmospheres. J Quant Spectrosc Radiat Transfer 1989;42:539–50. doi:10.1016/0022-4073(89)90044-7.

[40] Fu Q, Liou KN. On the correlated k -distribution method for radiative transfer in nonhomogeneous atmospheres. J Atmos Sci 1992;49:2139–56. doi:10.1175/1520-0469(1992)049<2139:OTCDMF>2.0.CO;2.

[41] Edwards DP, Francis GL. Improvements to the correlated- k radiative transfer method: Application to satellite infrared sounding. J Geophys Res 2000;105:18135–56. doi:10.1029/2000JD900131.

[42] Sekiguchi M, Nakajima T. A k-distribution-based radiation code and its computational optimization for an atmospheric general circulation model. J Quant Spectrosc Radiat Transf 2008;109:2779–93. doi:10.1016/j.jqsrt.2008.07.013.

[43] McMillin LM, Crone LJ, Kleespies TJ. Atmospheric transmittance of an absorbing gas 5 Improvements to the optran approach. Appl Opt 1995;34:8396. doi:10.1364/AO.34.008396.

[44] Matricardi M, Saunders R. Fast radiative transfer model for simulation of infrared atmospheric sounding interferometer radiances. Appl Opt 1999;38:5679. doi:10.1364/AO.38.005679.

[45] Min Q, Duan M. A successive order of scattering model for solving vector radiative transfer in the atmosphere. J Quant Spectrosc Radiat Transfer 2004;87:243–59. doi:10.1016/j.jqsrt.2003.12.019.

[46] Lenoble J, Herman M, Deuzé JL, Lafrance B, Santer R, Tanré D. A successive order of scattering code for solving the vector equation of transfer in the earth's atmosphere with aerosols. J Quant Spectrosc Radiat Transfer 2007;107:479–507. doi:10.1016/j.jqsrt.2007.03.010.

[47] Zhai P-W, Hu Y, Chowdhary J, Trepte CR, Lucker PL, Josset DB. A vector radiative transfer model for coupled atmosphere and ocean systems with a rough interface. J Quant Spectrosc Radiat Transfer 2010;111:1025–40. doi:10.1016/j.jqsrt.2009.12.005.

[48] de Haan JF, Bosma PB, Hovenier JW. The adding method for multiple scattering calculations of polarized light. Astron Astrophys 1987;183:371–91.

[49] Evans KF, Stephens GL. A new polarized atmospheric radiative transfer model. J Quant Spectrosc Radiat Transfer 1991;46:413–23. doi:10.1016/0022-4073(91)90043-P.

[50] Hovenier JW, Van Der Mee C, Domke H. Transfer of polarized light in planetary atmospheres: Basic concepts and practical methods. Dordrecht, Netherlands: Kluwer Academic Publishers; 2004.

[51] Siewert CE. A discrete-ordinates solution for radiative-transfer models that include polarization effects. J Quant Spectrosc Radiat Transfer 2000;64:227–54. doi:10.1016/S0022-4073(99)00006-0.

[52] Rozanov VV, Kokhanovsky AA. The solution of the vector radiative transfer equation using the discrete ordinates technique: Selected applications. Atmos Res 2006;79:241–65. doi:10.1016/j.atmosres.2005.06.006.

[53] Ota Y, Higurashi A, Nakajima T, Yokota T. Matrix formulations of radiative transfer including the polarization effect in a coupled atmosphere–ocean system. J Quant Spectrosc Radiat Transfer 2010;111:878–94. doi:10.1016/j.jqsrt.2009.11.021.

[54] Sommersten ER, Lotsberg JK, Stamnes K, Stamnes JJ. Discrete ordinate and Monte Carlo simulations for polarized radiative transfer in a coupled system consisting of two media with different refractive indices. J Quant Spectrosc Radiat Transf 2010;111:616–33. doi:10.1016/j.jqsrt.2009.10.021.

[55] Cohen D, Stamnes S, Tanikawa T, Sommersten ER, Stamnes JJ, Lotsberg JK, et al. Comparison of discrete ordinate and Monte Carlo simulations of polarized radiative transfer in two coupled slabs with different refractive indices. Opt Express 2013;21:9592. doi:10.1364/OE.21.009592.

[56] Stamnes S, Ou SC, Lin Z, Takano Y, Tsay SC, Liou KN, et al. Polarized radiative transfer of a cirrus cloud consisting of randomly oriented hexagonal ice crystals: The 3×3 approximation for non-spherical particles. J Quant Spectrosc Radiat Transf 2017;193:57–68. doi:10.1016/j.jqsrt.2016.07.001.

[57] Spurr RJD. VLIDORT: A linearized pseudo-spherical vector discrete ordinate radiative transfer code for forward model and retrieval studies in multilayer multiple scattering media. J Quant Spectrosc Radiat Transfer 2006;102:316–42. doi:10.1016/j.jqsrt.2006.05.005.

[58] Tynes HH, Kattawar GW, Zege EP, Katsev IL, Prikhach AS, Chaikovskaya LI. Monte Carlo and multicomponent approximation methods for vector radiative transfer by use of effective Mueller matrix calculations. Appl Opt 2001;40:400. doi:10.1364/AO.40.000400.

[59] Emde C, Buras R, Mayer B. ALIS: An efficient method to compute high spectral resolution polarized solar radiances using the Monte Carlo approach. J Quant Spectrosc Radiat Transfer 2011;112:1622–31. doi:10.1016/j.jqsrt.2011.03.018.

[60] Huang X, Yang P, Kattawar G, Liou K-N. Effect of mineral dust aerosol aspect ratio on polarized reflectance. J Quant Spectrosc Radiat Transfer 2015;151:97–109. doi:10.1016/j.jqsrt.2014.09.014.

[61] Wendisch M, Yang P. Theory of atmospheric radiative transfer: A compresensive introduction. Weinheim, Germany: Wiley-VCH; 2012.

[62] Potter JF. The Delta function approximation in radiative transfer theory. J Atmos Sci 1970;27:943–9. doi:10.1175/1520-0469(1970)027<0943:TDFAIR>2.0.CO;2.

[63] Wiscombe WJ. The Delta– M method: Rapid yet accurate radiative flux calculations for strongly asymmetric phase functions. J Atmos Sci 1977;34:1408–22. doi:10.1175/1520-0469(1977)034<1408:TDMRYA>2.0.CO;2.

[64] Hu Y-X, Wielicki B, Lin B, Gibson G, Tsay S-C, Stamnes K, et al. δ-Fit: A fast and accurate treatment of particle scattering phase functions with weighted singular-value decomposition least-squares fitting. J Quant Spectrosc Radiat Transfer 2000;65:681–90. doi:10.1016/S0022-4073(99)00147-8.

[65] Lin Z, Chen N, Fan Y, Li W, Stamnes K, Stamnes S. New Treatment of Strongly Anisotropic Scattering Phase Functions: The Delta- M + Method. J Atmos Sci 2018;75:327–36. doi:10.1175/JAS-D-17-0233.1.

[66] Zhai P-W, Hu Y, Trepte CR, Lucker PL. A vector radiative transfer model for coupled atmosphere and ocean systems based on successive order of scattering method. Opt Express 2009;17:2057. doi:10.1364/OE.17.002057.

[67] Sanghavi S, Stephens G. Adaptation of the delta- m and δ -fit truncation methods to vector radiative transfer: Effect of truncation on radiative transfer accuracy. J Quant Spectrosc Radiat Transfer 2015;159:53–68. doi:10.1016/j.jqsrt.2015.03.007.

[68] Hioki S, Yang P, Kattawar GW, Hu Y. Truncation of the scattering phase matrix for vector radiative transfer simulation. J Quant Spectrosc Radiat Transfer 2016;183:70–7. doi:10.1016/j.jqsrt.2016.06.011.

[69] Nakajima T, Tanaka M. Algorithms for radiative intensity calculations in moderately thick atmospheres using a truncation approximation. J Quant Spectrosc Radiat Transfer 1988;40:51–69. doi:10.1016/0022-4073(88)90031-3.

[70] Iwabuchi H, Suzuki T. Fast and accurate radiance calculations using truncation approximation for anisotropic scattering phase functions. J Quant Spectrosc Radiat Transf 2009;110:1926–39. doi:10.1016/j.jqsrt.2009.04.006.

[71] Rozanov V V., Lyapustin AI. Similarity of radiative transfer equation: Error analysis of phase function truncation techniques. J Quant Spectrosc Radiat Transf 2010;111:1964–79. doi:10.1016/j.jqsrt.2010.03.018.

[72] Cureton GP. Retrieval of higher order ocean spectral information from sunglint. IEEE Trans Geosci Remote Sens 2015;53:36–50. doi:10.1109/TGRS.2014.2317477.

[73] Ottaviani M, Knobelspiesse K, Cairns B, Mishchenko M. Information content of aerosol retrievals in the sunglint region. Geophys Res Lett 2013;40:631–4. doi:10.1002/grl.50148.

[74] Kaufman YJ, Martins J V., Remer LA, Schoeberl MR, Yamasoe MA. Satellite retrieval of aerosol absorption over the oceans using sunglint. Geophys Res Lett 2002;29:34-1-34–4. doi:10.1029/2002GL015403.

[75] Lu Y, Zhou Y, Liu Y, Mao Z, Qian W, Wang M, et al. Using remote sensing to detect the polarized sunglint reflected from oil slicks beyond the critical angle. J Geophys Res Ocean 2017;122:6342–54. doi:10.1002/2017JC012793.

[76] Kattawar GW, Adams CN. Stokes vector calculations of the submarine light field in an atmosphere-ocean with scattering according to a Rayleigh phase matrix: Effect of interface refractive index on radiance and polarization. Limnol Oceanogr 1989;34:1453–72. doi:10.4319/lo.1989.34.8.1453.

[77] Lin Z, Li W, Gatebe C, Poudyal R, Stamnes K. Radiative transfer simulations of the two-dimensional ocean glint reflectance and determination of the sea surface roughness. Appl Opt 2016;55:1206. doi:10.1364/AO.55.001206.

[78] Sun B, Kattawar GW, Yang P, Mlawer E. An improved small-angle approximation for forward scattering and its use in a fast two-component radiative transfer method. J Atmos Sci 2017;74:1959–87. doi:10.1175/JAS-D-16-0278.1.

[79] Wiscombe WJ. Extension of the doubling method to inhomogeneous sources. J Quant Spectrosc Radiat Transfer 1976;16:477–89. doi:10.1016/0022-4073(76)90083-2.

[80] Heidinger AK, O'Dell C, Bennartz R, Greenwald T. The successive-order-of-interaction radiative transfer model. Part I: Model development. J Appl Meteor Climatol 2006;45:1388–402. doi:10.1175/JAM2387.1.

[81] Liu Q, Weng F. Advanced Doubling–Adding method for radiative transfer in planetary atmospheres. J Atmos Sci 2006;63:3459–65. doi:10.1175/JAS3808.1.

[82] Zhai P-W, Hu Y, Winker DM, Franz BA, Werdell J, Boss E. Vector radiative transfer model for coupled atmosphere and ocean systems including inelastic sources in ocean waters. Opt Express 2017;25:A223. doi:10.1364/OE.25.00A223.

[83] Chami M, Lafrance B, Fougnie B, Chowdhary J, Harmel T, Waquet F. OSOAA: A vector radiative transfer model of coupled atmosphere-ocean system for a rough sea surface application to the estimates of the directional variations of the water leaving reflectance to better process multi-angular satellite sensors data over the. Opt Express 2015;23:27829. doi:10.1364/OE.23.027829.

[84] He X, Bai Y, Zhu Q, Gong F. A vector radiative transfer model of coupled ocean-atmosphere system using matrix-operator method for rough sea-surface. J Quant Spectrosc Radiat Transfer 2010;111:1426–48. doi:10.1016/j.jqsrt.2010.02.014.

[85] MODIS parameter. https://mcst.gsfc.nasa.gov/calibration/parameters (accessed August 13, 2019).

[86] Borbas EE, Seemann SW, Huang H-L, Li J, Menzel WP. Global profile training database for satellite regression retrievals with estimates of skin temperature and emissivity. Proc XIV Int ATOVS Study Conf 2005:763–70.

[87] Ding J. A fast vector radiative transfer model for polarimetric remote sensing. PhD thesis, Texas A&M University, College Station TX; 2019.

[88] Liou K-N. An introduction to atmospheric radiation. San Diego, CA: Academic Press; 2002.

[89] Kokhanovsky AA, Budak VP, Cornet C, Duan M, Emde C, Katsev IL, et al. Benchmark results in vector atmospheric radiative transfer. J Quant Spectrosc Radiat Transfer 2010;111:1931–46. doi:10.1016/j.jqsrt.2010.03.005.

[90] PACE Ocean Color Instrument n.d. https://pace.oceansciences.org/oci.htm (accessed August 14, 2019).

[91] Hasekamp OP, Fu G, Rusli SP, Wu L, Di Noia A, Brugh J aan de, et al. Aerosol measurements by SPEXone on the NASA PACE mission: expected retrieval capabilities. J Quant Spectrosc Radiat Transf 2019;227:170–84. doi:10.1016/j.jqsrt.2019.02.006.

[92] Platnick S, Meyer KG, King MD, Wind G, Amarasinghe N, Marchant B, et al. The MODIS Cloud Optical and Microphysical Products: Collection 6 updates and examples from Terra and Aqua. IEEE Trans Geosci Remote Sens 2017;55:502–25. doi:10.1109/TGRS.2016.2610522.

[93] Yang P, Bi L, Baum BA, Liou K-N, Kattawar GW, Mishchenko MI, et al. Spectrally consistent scattering, absorption, and polarization properties of atmospheric ice crystals at wavelengths from 0.2 to 100 μ m. J Atmos Sci 2013;70:330–47. doi:10.1175/JAS-D-12-039.1.

[94] Yang P, Ding J, Panetta RL, Liou K, Kattawar GW, Mishchenko M. On the convergence of numerical computations for both exact and approximate solutions for electromagnetic scattering by nonspherical dielectric particles. Prog Electromagn Res 2019;164:27–61.

[95] Stegmann PG, Yang P. A regional, size-dependent, and causal effective medium model for Asian and Saharan mineral dust refractive index spectra. J Aerosol Sci 2017;114:327–41. doi:10.1016/j.jaerosci.2017.10.003.

[96] Bi L, Yang P. Accurate simulation of the optical properties of atmospheric ice crystals with the invariant imbedding T-matrix method. J Quant Spectrosc Radiat Transfer 2014;138:17–35. doi:10.1016/j.jqsrt.2014.01.013.

[97] Sun B, Yang P, Kattawar GW, Zhang X. Physical-geometric optics method for large size faceted particles. Opt Express 2017;25:24044. doi:10.1364/OE.25.024044.

[98] Stamnes K, Tsay S-C, Wiscombe W, Jayaweera K. Numerically stable algorithm for discrete-ordinate-method radiative transfer in multiple scattering and emitting layered media. Appl Opt 1988;27:2502. doi:10.1364/AO.27.002502.

[99] Cox C, Munk W. Measurement of the roughness of the sea surface from photographs of the sun's glitter. J Opt Soc Am 1954;44:838. doi:10.1364/JOSA.44.000838.

[100] Morel A, Prieur L. Analysis of variations in ocean color1. Limnol Oceanogr 1977;22:709–22. doi:10.4319/lo.1977.22.4.0709.

[101] Bricaud A, Babin M, Morel A, Claustre H. Variability in the chlorophyll-specific absorption coefficients of natural phytoplankton: Analysis and parameterization. J Geophys Res 1995;100:13321. doi:10.1029/95JC00463.

[102] Bricaud A, Morel A, Babin M, Allali K, Claustre H. Variations of light absorption by suspended particles with chlorophyll a concentration in oceanic (case 1) waters: Analysis

and implications for bio-optical models. J Geophys Res Ocean 1998;103:31033–44. doi:10.1029/98JC02712.

[103] Bricaud A, Morel A, Prieur L. Absorption by dissolved organic matter of the sea (yellow substance) in the UV and visible domains1. Limnol Oceanogr 1981;26:43–53. doi:10.4319/lo.1981.26.1.0043.

[104] Loisel H, Morel A. Light scattering and chlorophyll concentration in case 1 waters: A reexamination. Limnol Oceanogr 1998;43:847–58. doi:10.4319/lo.1998.43.5.0847.

[105] Morel A, Maritorena S. Bio-optical properties of oceanic waters: A reappraisal. J Geophys Res Ocean 2001;106:7163–80. doi:10.1029/2000JC000319.

[106] Huot Y, Morel A, Twardowski MS, Stramski D, Reynolds RA. Particle optical backscattering along a chlorophyll gradient in the upper layer of the eastern South Pacific Ocean. Biogeosciences 2008;5:495–507. doi:10.5194/bg-5-495-2008.

[107] Pope RM, Fry ES. Absorption spectrum (380–700 nm) of pure water II Integrating cavity measurements. Appl Opt 1997;36:8710. doi:10.1364/AO.36.008710.

[108] Mobley CD. Light and water: Radiative transfer in natural waters. San Diego, CA: Academic Press; 1994.

[109] Xu G, Sun B, Brooks SD, Yang P, Kattawar GW, Zhang X. Modeling the inherent optical properties of aquatic particles using an irregular hexahedral ensemble. J Quant Spectrosc Radiat Transfer 2017;191:30–9. doi:10.1016/j.jqsrt.2017.01.020.

[110] Chowdhary J, Cairns B, Waquet F, Knobelspiesse K, Ottaviani M, Redemann J, et al. Sensitivity of multiangle, multispectral polarimetric remote sensing over open oceans to water-leaving radiance: Analyses of RSP data acquired during the MILAGRO campaign. Remote Sens Environ 2012;118:284–308. doi:10.1016/j.rse.2011.11.003.

[111] Zhang X, Gray DJ. Backscattering by very small particles in coastal waters. J Geophys Res Ocean 2015;120:6914–26. doi:10.1002/2015JC010936.

[112] Zhang X, Stavn RH, Falster AU, Rick JJ, Gray D, Gould RW. Size distributions of coastal ocean suspended particulate inorganic matter: Amorphous silica and clay minerals and their dynamics. Estuar Coast Shelf Sci 2017;189:243–51. doi:10.1016/j.ecss.2017.03.025.

[113] Fougnie B, Bracco G, Lafrance B, Ruffel C, Hagolle O, Tinel C. PARASOL in-flight calibration and performance. Appl Opt 2007;46:5435. doi:10.1364/AO.46.005435.

[114] Gelaro R, McCarty W, Suárez MJ, Todling R, Molod A, Takacs L, et al. The Modern-Era Retrospective Analysis for Research and Applications, Version 2 (MERRA-2). J Clim 2017;30:5419–54. doi:10.1175/JCLI-D-16-0758.1.

[115] Bodhaine BA, Wood NB, Dutton EG, Slusser JR. On Rayleigh optical depth calculations. J Atmos Ocean Technol 1999;16:1854–61. doi:10.1175/1520-0426(1999)016<1854:ORODC>2.0.CO;2.